

Natural hydrogen potential and basaltic alteration in the Asal–Ghoubbet rift, Republic of Djibouti.

Gabriel Pasquet^{1,*} , Amin Mohamed Idriss^{1,2}, Lou Ronjon-Magand³, Magali Ranchou-Peyruse^{3,4} , Marion Guignard³ , Mathieu Duttine⁵, Anthony Ranchou-Peyruse³  and Isabelle Moretti¹ 

¹ Université de Pau et des Pays de l'Adour, E2S UPPA, LFCR, Pau, France

² Office djiboutien de développement de l'énergie géothermique (ODDEG), Djibouti, Djibouti

³ Université de Pau et des Pays de l'Adour, E2S UPPA, CNRS, IPREM, Pau, France

⁴ Université de Pau et des Pays de l'Adour, E2S UPPA, LaTEP, Pau, France

⁵ Institut de chimie de la matière condensée de Bordeaux (ICMCB), Université de Bordeaux, UMR 5026, 33600 Pessac, France

Received: 7 December 2022 / Accepted: 27 March 2023 / Publishing online: 1 June 2023

Abstract – The Asal–Ghoubbet active rift in the Republic of Djibouti is a site of interest for geothermal energy and natural hydrogen, and previous studies have indicated that dihydrogen (H₂) emanates from this rift. However, the well-known serpentinization reaction does not appear to be the main mechanism generating H₂ at this site. Rather, the H₂ is generated as follows: (1) by alteration of basaltic lava at depth *via* reaction with seawater flowing from Ghoubbet Bay towards Lake Asal; (2) by simple degassing of the volcanic chamber located a few kilometers below the Fiale Caldera in the rift axis; or (3) as a result of pyritization processes *via* the oxidation of H₂S. Study of microorganisms did not indicate any production or consumption of H₂, CO₂, or CH₄; therefore, it is unlikely that microorganisms affected H₂ gas contents measured at the surface. However, air contamination at fumaroles is typically considerable and may limit interpretation of such processes. Drill cuttings from the Fiale 1 (F1) and Gale le Goma 1 (Glc1) wells (located on the inner and outer rift margins, respectively) were analyzed to determine where H₂ is generated. Total rock analyses indicated distinct zones at depths of 464 m and 280 m for F1 and Glc1, respectively, representing the boundary between the Asal and Stratoid Basalts. ⁵⁷Fe Mössbauer analyses show a decrease in the percentage of Fe³⁺ at depth, indicating that Fe²⁺-rich minerals, particularly in the Stratoid Basalts, may be a source of H₂. Based on well data from the rift center and the outer rift margin, it is evident that H₂ is present at the surface in the rift axis and that this area offers good remnant potential because of the presence of Fe-rich chlorite. Conversely, few H₂ emissions were measured at the surface on the outer rift margins, although well data showed some H₂ (~0.25%) at depth. The presence of a cap rock in the rift axis has not yet been proven; however, the high loss on ignition and the mineralogy in well Glc1 may indicate that the rocks are sufficiently altered into clays to offer potential as a H₂ seal. If so, the rift margins would offer greater exploration potential than the rift center.

Keywords: natural hydrogen / geothermal energy / Djibouti / Asal Rift / alteration / basalts

Résumé – Potentiel en hydrogène naturel et altération basaltique dans le rift d'Asal–Ghoubbet, République de Djibouti. Le rift actif d'Asal–Ghoubbet en République de Djibouti est un site d'intérêt pour l'énergie géothermique et l'hydrogène naturel, et des études précédentes ont indiqué que du dihydrogène (H₂) émane de ce rift. Cependant, la réaction de serpentinisation bien connue ne semble pas être le principal mécanisme de production de H₂ sur ce site. L'H₂ est plutôt généré de la manière suivante : (1) par altération de la lave basaltique en profondeur *via* une réaction avec l'eau de mer s'écoulant de la baie de Ghoubbet vers le lac Asal ; (2) par simple dégazage de la chambre volcanique située à quelques kilomètres sous la caldeira de Fiale dans l'axe du rift ; ou (3) à la suite de processus de pyritisation *via* l'oxydation de H₂S. L'étude des micro-organismes n'a pas indiqué de production ou de consommation de H₂, CO₂ ou CH₄ ; il est donc peu probable que les micro-organismes aient affecté les teneurs en gaz H₂ mesurées à la surface. Cependant, la contamination de l'air dans les fumerolles est généralement considérable et peut limiter l'interprétation de

*Corresponding author: gabriel.pasquet@univ-pau.fr

tels processus. Les déblais de forage des puits Fiale 1 (F1) et Gale le Goma 1 (Glc1) (situés respectivement sur les marges intérieure et extérieure du rift) ont été analysés pour déterminer où l'H₂ est généré. Les analyses de la roche totale ont indiqué des zones distinctes à des profondeurs de 464 m et 280 m pour F1 et Glc1, respectivement, représentant la limite entre les basaltes d'Asal et Stratoïd. Les analyses ⁵⁷Fe Mössbauer montrent une diminution du pourcentage de Fe³⁺ en profondeur, ce qui indique que les minéraux riches en Fe²⁺, notamment dans les basaltes Stratoïd, peuvent être une source de H₂. D'après les données des puits du centre du rift et de la marge externe du rift, il est évident que l'H₂ est présent à la surface dans l'axe du rift et que cette zone offre un bon potentiel rémanent en raison de la présence de chlorite riche en Fe. À l'inverse, peu d'émissions d'H₂ ont été mesurées à la surface sur les marges extérieures du rift, bien que les données de puits aient montré la présence d'H₂ (~0,25 %) en profondeur. La présence d'une roche de couverture dans l'axe du rift n'a pas encore été prouvée ; cependant, la forte perte au feu et la minéralogie dans le puits Glc1 peuvent indiquer que les roches sont suffisamment altérées sous forme argileuse pour offrir un potentiel en tant que couverture à l'H₂. Si tel est le cas, les marges du rift offrirait un plus grand potentiel d'exploration que le centre du rift.

Mots clés : hydrogène naturel / géothermie / Djibouti / Rift d'Asal / altération / basaltes

1 Introduction

Dihydrogen (H₂) is a key element in the energy transition and is often used as an energy carrier (*e.g.*, for storage) rather than as a primary energy source (Moretti, 2019; Lapi *et al.*, 2022). At present, H₂ is produced primarily from hydrocarbons through a process that emits high volumes of CO₂; this is known as “grey” hydrogen (Rigollet and Prinzhofer, 2022). However, lower emission sources of H₂ exist and are more appropriate in the context of current global environmental conditions. Dihydrogen is referred to as “blue” when CO₂ emissions are captured and stored during grey hydrogen processing and as “green” when it is produced by the electrolysis of water using a decarbonized source of electricity. “White” dihydrogen is H₂ in its natural state (Rigollet and Prinzhofer, 2022) and is generated mainly through fluid rock interactions reactions (Smith *et al.*, 2005; Gaucher, 2020; Moretti and Webber, 2021).

This natural H₂ has been observed in various geological contexts (Truche *et al.*, 2020; Zgonnik, 2020), including mid-oceanic ridges (Charlou *et al.*, 1998, 2002; Kelley *et al.*, 2001; Kelley, 2005); ophiolitic massifs such as the Sultanate of Oman, New Caledonia, or the Philippines (Neal and Stanger, 1983; Abrajano *et al.*, 1988; Sano *et al.*, 1993; Deville and Prinzhofer, 2016; Vacquand *et al.*, 2018); and Archean and Proterozoic cratonic basins such as those in Namibia, Mali, Russia, Australia, and Brazil (Larin *et al.*, 2015; Prinzhofer *et al.*, 2018, 2019; Boreham *et al.*, 2021; Moretti *et al.*, 2021, 2022; Malvoisin and Brunet, 2023). Steam at the high-temperature geothermal sites of Italy, Iceland, and Djibouti (Oskarsson, 1984; Ármannsson *et al.*, 1989; Leila *et al.*, 2021; Pasquet *et al.*, 2021, 2022; Combaudon *et al.*, 2022) has also been shown to contain H₂, possibly from multiple sources.

Many H₂ emission zones have been discovered, yet the production of natural hydrogen (as in Mali; Prinzhofer *et al.*, 2018) remains rare and natural H₂ exploration is still in its infancy. The geological and geothermal context of the active rift in the Afar Depression is favorable for natural H₂ production, with several sources proposed previously: alteration of iron minerals in basaltic material, pyritization, or volcanic degassing (Holloway and O'Day, 2000; Klein *et al.*, 2020; Pasquet *et al.*, 2021). Following surface gas surveys,

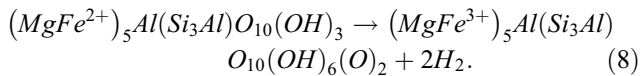
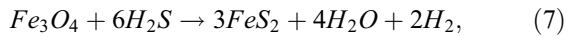
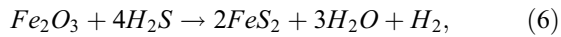
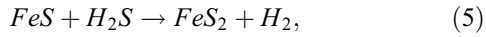
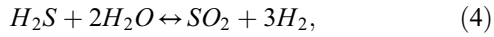
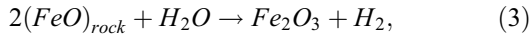
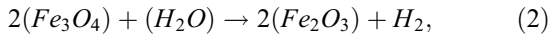
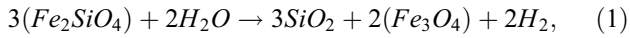
analysis of cuttings from two wells is presented below and aims to improve our understanding of basalt alteration and Fe²⁺/Fe³⁺ evolution at depth across the Asal–Ghoubbet rift in order to assess its potential H₂ resource.

1.1 Hydrogen system

Many reactions can produce H₂ (Worman *et al.*, 2020), depending on the protolith, fluid, and physical parameters (*i.e.*, temperature, pressure) of the environment; some of these reactions are oxidation–reduction processes. The ferrous iron contained in a mineral is oxidized when in contact with water to become ferric iron, whereas the water is reduced to form H₂. The more ferrous iron a rock contains, the greater its ability to produce H₂ during alteration processes. Basalt is composed mainly of plagioclase, with smaller amounts of pyroxene and olivine (olivine typically less than 20%). Olivine, including the iron-rich end-member fayalite, is highly unstable at the surface and will deteriorate more rapidly than the other minerals present in basalt (Stevens and McKinley, 2000; Sissmann *et al.*, 2014; Kularatne *et al.*, 2018). In contrast, plagioclase, the major phase, has less or no iron and is kinetically more stable. Accordingly, the production of H₂ from a basaltic protolith is typically limited by its high plagioclase content.

Despite this limitation, volcanic zones such as Iceland (Combaudon *et al.*, 2022) offer other advantages for natural hydrogen production. These include the relatively regular renewal of crustal material (and thus of potentially oxidizable minerals), high temperature gradient, significant water resource (meteoric, glacial, or marine), and production of H₂S due to volcanic activity.

The present study will focus on several oxidation–reduction equations that generate H₂: oxidation of Fe²⁺ from fayalite to magnetite (eq. (1)); oxidation of Fe²⁺ from magnetite to hematite (eq. (2)); oxidation of Fe²⁺ from mesostasis to hematite (eq. (3)); oxidation from H₂S to SO₂ in the gas phase (eq. (4)); iron sulphides pyritization (eq. (5)); oxidation of H₂S to form pyrite from hematite (eq. (6)) and magnetite (eq. (7)) (Arrouvel and Prinzhofer, 2021); and oxidation of chlorite from Fe²⁺ to Fe³⁺ (eq. (8)) (Steudel *et al.*, 2016; Lempart *et al.*, 2018).



Additionally, different clay phases can be formed by basalt alteration at different temperatures, with smectites at low temperatures and chlorites at higher temperatures. This argillization of basalt does not necessarily lead to direct production of H_2 , because the iron remains ferrous (Reed and Palandri, 2008). However, once chlorite is formed, it can oxidize (Brindley and Youell, 1953); here, we discuss whether this could represent an intermediary phase for H_2 production. As in hydrocarbon systems, in addition to defining the source rock (here, the reactive minerals) for H_2 generation, it is also necessary to define a reservoir, migration pathways, and a seal.

1.2 The Asal–Ghoubbet context

1.2.1 Geological context

The Asal–Ghoubbet rift is part of a large spreading system, the East African Rift (EAR), that extends from the Red Sea in the north to Mozambique in the south. In the Republic of Djibouti (Fig. 1), in the north of the magmatic east branch of the EAR, this rift is an emergent segment of the Aden Ridge (Stieltjes *et al.*, 1976). Although continental extension started earlier, the first evidence of oceanic crust accretion in the Gulf of Aden has been dated to 20–17 Ma (Nonn *et al.*, 2017, 2019). In the Red Sea, extension started approximately 25 Ma and ocean formation approximately 4 Ma. In the southern Red Sea, Gulf of Aden, and Afar region, after various phases of extension, volcanism, and thinning (Barberi *et al.*, 1972, 1975b), a large series of fissural basaltic eruptions resulted in the Afar Stratoid Series (Barberi *et al.*, 1975a). This series is composed of basalts with an alkaline tendency (Varet, 1978; Fournier *et al.*, 1984) at its base and rhyolitic rocks at its top and has been dated to 4–1 Ma. These eruptions were followed by the Axial Series, from 1 Ma to the present day; this series comprises more evolved tholeiitic and porphyritic basalts. These series represent the accretionary segments of the present axial volcanic ranges, linked together by transform faults, such

as the Asal–Ghoubbet rift (Barberi and Varet, 1970; Stieltjes *et al.*, 1976; Barberi and Varet, 1977). The N130° oriented Asal–Ghoubbet rift has an opening rate of approximately 1.5–2 cm/year (Delibrias *et al.*, 1975) with a N40° direction. The last major eruption in the rift zone was that of the Ardoukoba shield volcano in 1978 (Demange *et al.*, 1980). The rift comprises three main zones: the axial volcanic zone, the inner margins, and the outer margins. The lavas evolve from porphyritic on the margins to aphyritic in the center and from magnesian to ferrous towards the center of the rift zone (Stieltjes *et al.*, 1976; Varet, 1978).

1.2.2 Geothermal exploration

The geodynamic activity of this rift has prompted numerous geothermal exploration campaigns since the 1970s, and temperatures observed in exploration wells have been encouraging with an average thermal gradient of 180°C/km to 200°C/km in the axis as on the margins. In 1975, the BRGM (Bureau de recherches géologiques et minières) drilled two wells on the southwestern outer margin of the rift: wells A1 (260°C) and A2 were drilled to depths of 1154 and 1554 m, respectively (Abdillahi, 2014). A second phase of drilling, carried out by Aquater between 1987 and 1988, created three new wells on the outer margins of the rift: wells A3 ($T_{\text{max}}=265^\circ\text{C}$), A4 ($T_{\text{max}}=344^\circ\text{C}$), and A6 ($T_{\text{max}}=281^\circ\text{C}$) were drilled to depths of 1316, 2011, and 1761 m, respectively, while well A5 (located in the center of the rift) was drilled to 2105 m ($T_{\text{max}}=359^\circ\text{C}$) (D'Amore *et al.*, 1997; Abdillahi, 2014). Since 2016, further drilling has been undertaken in the rift: the Gale le Goma 1 (Glc1) well was drilled to 600 m on the southern outer margin near A3 and A1 ($T_{\text{max}}=138^\circ\text{C}$) (Ahmed, 2018); and, more recently, wells F1 ($T_{\text{max}}=363^\circ\text{C}$), F2 ($T_{\text{max}}=352^\circ\text{C}$), and F3 ($T_{\text{max}}=363^\circ\text{C}$) were drilled around the Fiale Caldera to depths of 2475, 2237, and 2402 m, respectively (Turk *et al.*, 2019).

Seismic velocity anomaly studies have identified a magma chamber beneath the Fiale Caldera at a depth of more than 5 km (Dubre *et al.*, 2007). Combined velocity anomaly data and well data indicate cold marine water intrusions between 0 and 1 km depth in the center of the rift (Zan *et al.*, 1990; Dubre *et al.*, 2007; Dubre and Peltzer, 2007). Seawater flows from Ghoubbet Bay to Lake Asal through numerous NW–SE faults. This temperature inversion at shallow depth has been noted in wells A5, F1, F2, and F3, *i.e.*, at the center of the rift (Zan *et al.*, 1990; Dubre *et al.*, 2007; Turk *et al.*, 2019). At the rift margins, these hypersaline fluids are warmer and the flow is weaker (Mlynarski and Zlotnicki, 2001).

1.2.3 H_2 in the Asal–Ghoubbet rift

Well data and a field campaign (2019) across the rift highlighted the presence of H_2 at depth in the area (Fig. 2), in some geothermal wells along the southwestern margin (wells A3 and A6; D'Amore *et al.*, 1997), and in the fumaroles along the southern inner margin near well A5 and the Fiale Caldera (Pasquet *et al.*, 2021). The well data indicate H_2 percentages of ~0.25% (in dry gas, excluding air and water vapor); however, no H_2 sources were measured at the surface in the vicinity of the wells during the field campaign. Along the inner margins and in the axial volcanic zone, although no gas data were

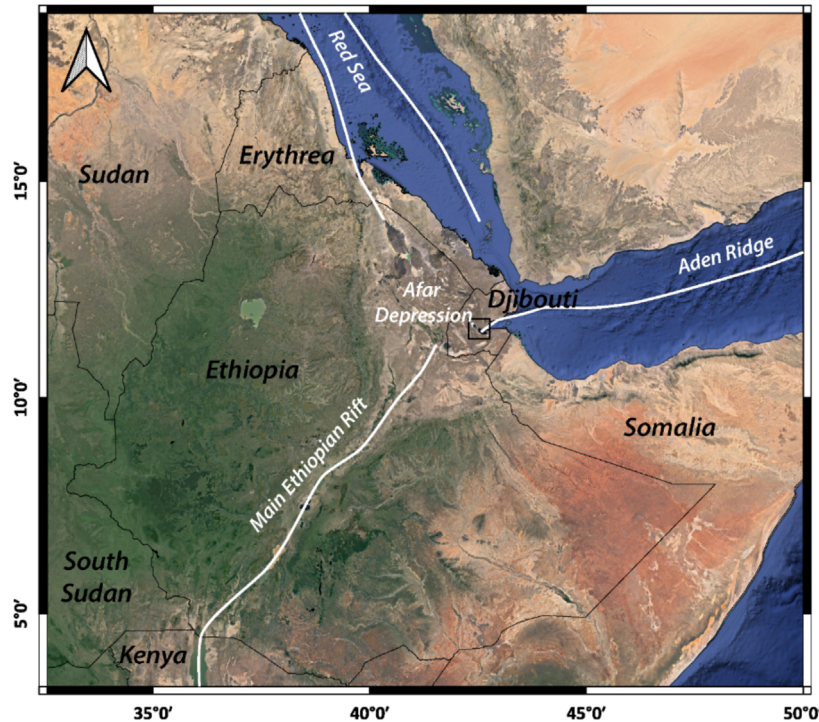


Fig. 1. Map representing the major opening axes of the EARS, with the Asal–Ghoubbet rift (study area) indicated by black box.

acquired at depth, the intense hydrothermal activity present at the surface made it possible to measure gas contents: after correction for air, H_2 contents were found to be up to 3%, with an average value of 1% and a mean value of 0.77% (Pasquet *et al.*, 2021). Gas analysis following the 1978 Arduokoba eruption (in the volcanic core zone) also indicated 0.15% H_2 in the magma gas (Allard *et al.*, 1979). At the surface, H_2 concentrations were found to increase towards the center of the rift (Pasquet *et al.*, 2021).

Several hypotheses have been proposed for the origin of this H_2 : (1) alteration of basalts by hot hypersaline fluids circulating at depth; (2) alteration of basalts at lower temperatures due to marine intrusion at shallow depth in the rift axis; (3) pyritization; and (4) volcanic degassing as magma ascends through major active faults rooted near the magma chamber (Pasquet *et al.*, 2021).

In summary, H_2 has been measured at depth in geothermal wells along the margins of the Asal–Ghoubbet system but has not yet been detected at the surface in these areas. Conversely, in the center of the rift, H_2 has been measured at the surface in fumaroles but no subsurface data are available.

2 Materials and methods

We first conducted a preliminary analysis of surface gases in the axial volcanic zone. Gas measurements were acquired in the field during two campaigns in 2019 and 2020 using the BIOGAS 5000 analyzer; some of this dataset has been published previously (Pasquet *et al.*, 2021). Soil samples were acquired primarily during the first campaign in 2019, although one sample was acquired in 2021.

The drill cuttings from the Fiale 1 (F1) and Glc1 wells were studied based on total rock analysis: ICP–OES (Inductif Coupled Plasma Optical Emission Spectrometry), XRD (X-ray diffraction) and Mössbauer spectroscopy. The ICP–OES analyses were carried out by the Service d’analyse des roches et des minéraux of the CRPG at Nancy.

2.1 Gas sampling

Surface gas measurements were acquired on three different days. The studied site is located near the Asal 5 (A5) and F1 geothermal wells, along the inner margins of the rift along a major N140°-oriented fault that runs between Ghoubbet Bay and Lake Asal (Pasquet *et al.*, 2021; Pasquet, 2023). This site includes a set of fumaroles with hydrothermal alteration around them (Fig. 3). Steam is present over approximately 70 m wide and the Afar people living in this area have installed tubes to induce condensation and take advantage of the drinking water contained in the hot steam. To obtain measurements, a perforated stainless steel tube was inserted into the fumaroles; drilling tools were not necessary as the soil was soft. The tube was then connected by silicone tubes to the BIOGAS 5000 field analyzer. Also, to increase gas capture for fumaroles, a funnel can be placed in the vent and connected directly to the analyzer. Gas contents were monitored in real time, although only peak values for each 2-min interval were recorded. CH_4 , CO_2 , and O_2 were measured in % and H_2 , CO , and H_2S in ppm. The remaining unanalyzed gases were grouped under the term “Balance” and measured in %. This balance is often considered to be N_2 but might also include, in this volcanic context, gases such as SO_2 or HCl . $H_2O_{(g)}$ was not analyzed owing to the presence of a water vapor filter.

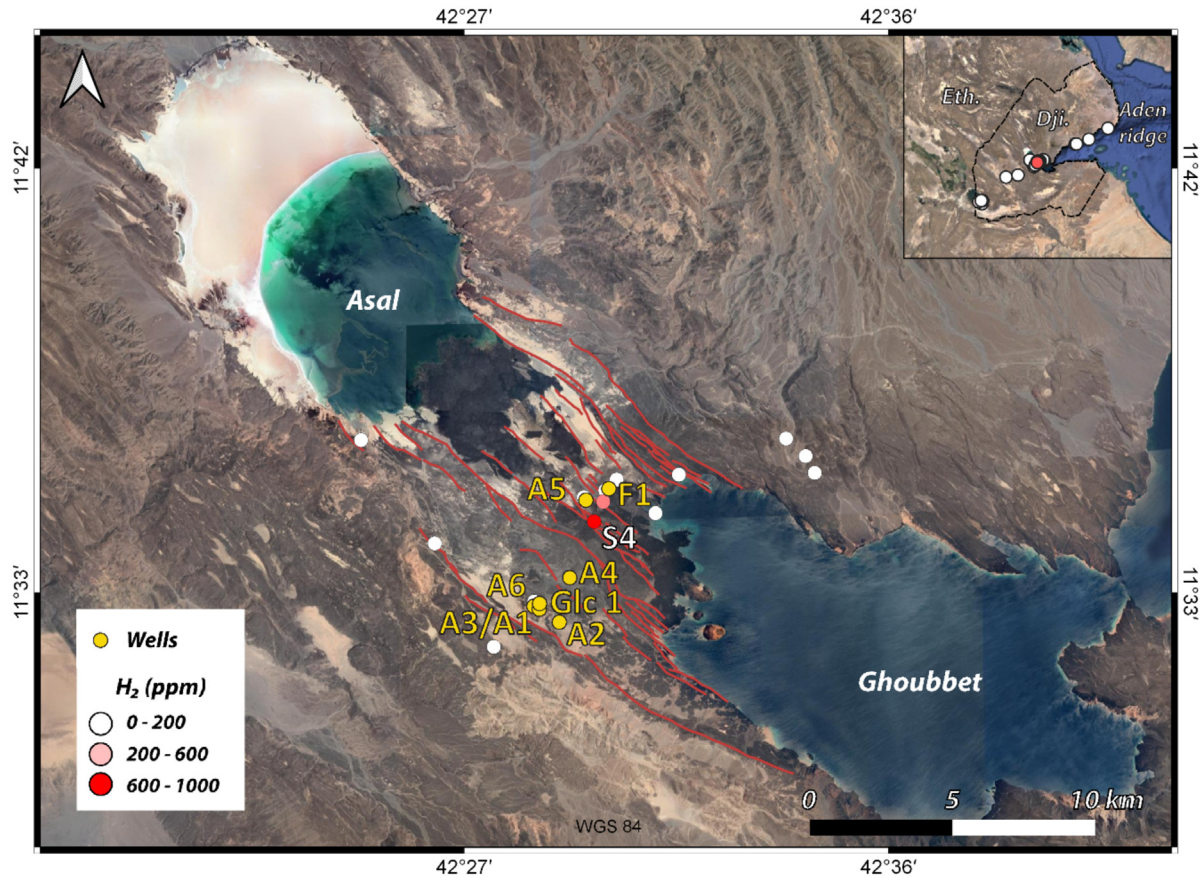


Fig. 2. Map of the Asal–Ghoubbet rift showing major rift faults, geothermal wells, and surface H₂ measurement points. The color scale from white to red indicates increasing H₂ contents in fumaroles at the site. The red dot corresponds to site no. 4, presented in [Figure 3](#).

Measurements uncertainties were as follows: $\pm 0.5\%$ of the CH₄ and CO₂ contents; $\pm 1.0\%$ of the O₂ content; $\pm 2.5\%$ of the H₂ content; and $\pm 2.0\%$ of the CO and H₂S contents.

As H₂ contents have been shown to vary both within and between days in some geological settings ([Prinzhofer et al., 2019](#); [Moretti et al., 2021, 2022](#)), we recorded the time each measurement was obtained and will present the results versus time. Although samples were obtained from various locations along the leaking zone ([Fig. 3](#)), no SE–NW trends in concentrations were noted; accordingly, we did not attempt to map H₂ concentrations spatially.

2.2 Microbiological approaches

H₂ can be an electron donor and an energy source for many aerobic, sulfate-reducing, (homo)acetogenic and methanogenic microorganisms. We identified the microbial families present and considered the metabolic processes associated and described in the literature, in particular their ability to consume H₂. Extraction of genomic DNA was performed on 250 mg of soil using the DNeasy PowerSoil Pro kit (Qiagen). gDNA was quantified by fluorescence, using the Quant-it kit (Invitrogen), following the supplier's instructions. A Synergy HTX multi-mode reader (BioTek) microplate reader using the Gen5 software was used. Amplifications of 16S rRNA genes were performed by PCR for soil diversity analysis

by Illumina MiSeq sequencing. Universal primers 515F-ill (CTTTCCCTACACGACGCTCTTCCGATCTGTGYCAGC-MGCCGCGGTA) and 928R-ill (GGAGTTCAGACGTGCT-CTCCGATCT CCCCGYCAATTCMTTTRAGT) (region V4–V5; [Wang et al., 2015](#)) were used, containing the tags required for sequencing, according to the following PCR cycle: 94 °C–2 min; (94 °C–30 s; 65 °C–30 s; 72 °C–40 s) \times 30; 72 °C–7 min. The core PCR kit (Roche) supplemented with 1 mg/mL (final concentration) of BSA (Bovine Serum Albumin, supplied by NEB-B9200S) was used, with a 2720 Thermal Cycler (Applied Biosystems). The amplicons were sequenced using the MiSeq Illumina 2 \times 250 bp technique, via the GenoToul sequencing platform (Toulouse, France) and analyzed with the FROGS analysis pipeline as described in [Haddad et al. \(2022\)](#). In order to monitor metabolic activity based on gas phase variations in soil samples from the 2021 Djibouti campaign, soil samples weighing 2 g were introduced into sterile 100 mL penicillin vials. Two conditions were defined: in anaerobiosis and in aerobiosis. The anoxic vials were hermetically sealed (butyl stopper, aluminum cap) and flushed with nitrogen; then, 10 mL of sterile nitrogen-degassed distilled water was added to the soil. Finally, these bottles were flushed with H₂/CO₂ (80/20; 1 bar). The oxic flasks were treated in the same way except for the initial gaseous phase, which was air and sterile distilled water that had not been degassed in order to maintain aerobic conditions. H₂/CO₂ was

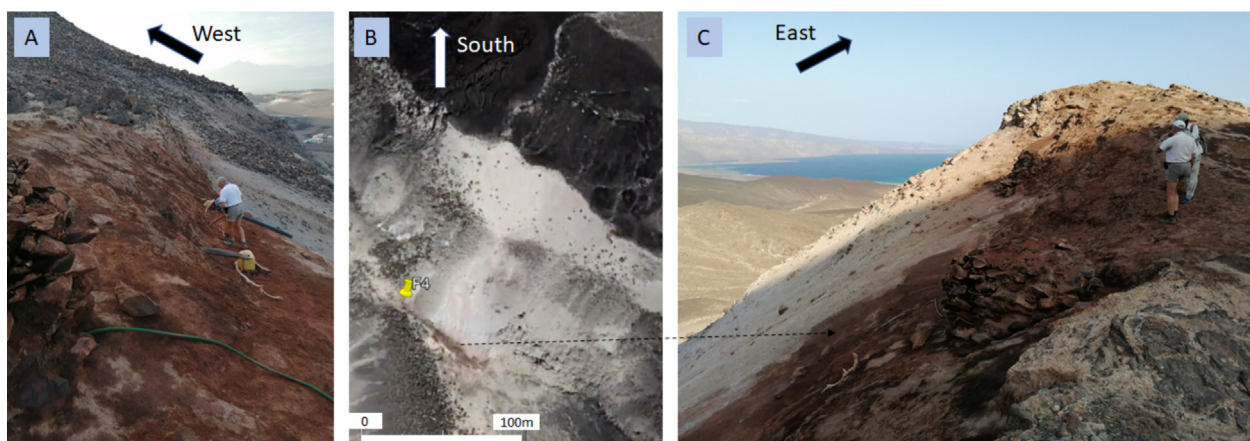


Fig. 3. Site 4 of the Asal–Ghoubbet rift. A. View towards the west and Lake Asal, showing plastic tubes installed by local inhabitants to collect fresh water. B. Satellite view, showing the area affected by the fumaroles with visible surface alteration in brown. C. View to Ghoubbet Bay, showing the eastern hydrothermal zone with numerous fumaroles and Afar condensation wells. The scarp of the N140°-oriented north-dipping normal fault clearly demonstrates the tectonic activity of this central part of the rift.

added under slight overpressure in the sealed bottles (1 bar). The vials were then incubated at 95 °C. After 10 days of incubation, the composition of the gaseous phase was again analyzed to compare the gaseous phases versus T0; in this way, we were able to monitor the evolution of the system (GC- μ TCD, Micro GC Fusion, Chemlys, France). The cultures were placed in an oven at 37 °C for 30 minutes before analysis and the pressure of the gaseous phase quantified before and after analysis by a manometer (Digitron 2022P) in order to quantify the moles of gases present under the same conditions.

Materials from two field campaigns (in 2019 and 2021) have been studied. Soil samples were collected in triplicate at Site 4 (Fig. 3). During the 2021 campaign, three locations along the leaking zone were sampled and named zones 13, 15 and 16.

2.3 XRD

The well cuttings were reduced to powder to obtain XRD measurements. The analyses were carried out at the Université de Pau et des Pays de l'Adour using a D2 PHASER diffractometer (Bruker). XRD allowed us to obtain information about the crystalline phases of our rock samples and thus to determine both qualitatively and quantitatively the presence of specific minerals. For this analysis, the powdered samples were mounted on a base and the intensity of scattered X-rays analyzed to determine mineral composition.

The analyses were performed under conditions of 10 mA, 300 W, and 30 kV and a PSD (Position Sensitive Detector) of 1.6 s. The front slot, blade, and back slot had openings at 0.2, 1.0, and 3.0 mm, respectively. The observed 2θ angle was between 10 and 80° with an X-ray wavelength of 1.54184 Å.

2.4 Mössbauer spectroscopy

Once the mineral phases were identified, their $\text{Fe}^{2+}/\text{Fe}^{3+}$ ratios were measured to determine potential for oxidation to produce H_2 . For this purpose, ^{57}Fe Mössbauer spectroscopic

analyses were carried out at the “Resonance Spectroscopies” facility of the Institute of Condensed Matter Chemistry of Bordeaux (ICMCB). This analysis is based on the Fe oxidation state, magnetic state, and crystalline chemistry of iron-containing minerals. In particular, it allows characterization of the valence of iron and the sites at which iron is present within crystals.

The measurements were carried out at room temperature using a constant acceleration spectrometer operating in transmission geometry. The gamma emitter used in the experimental setup is a ^{57}Co radioactive source (activity: 1.85 GBq) embedded in a rhodium matrix kept at room temperature (293 K). Thin absorbers were prepared with about 250 mg of sample powder and placed between the source of gamma rays and a NaI(Tl) scintillation detector. The recorded ^{57}Fe Mössbauer spectra are then the sum of various components (sub-spectra) associated with the different iron-bearing minerals in the analyzed rock samples. Each sub-spectrum is characterized by Mössbauer hyperfine parameters: isomer shift (δ , in mm/s, relative to $\alpha\text{-FeO}$ at room temperature), quadrupole splitting (Δ , in mm/s) or quadrupole shift (2ϵ , in mm/s), hyperfine magnetic field (B_{hf} , in T) and resonance line width (Γ , in mm/s). Refinement of hyperfine parameters and relative absorption areas were performed with the WinNormos® software (Wissenschaftliche Elektronik GmbH).

3 Results

Here, we present our results based on the analysis of *in situ* gas measurements obtained at Site 4 (Fig. 3). This fumarole site ($T > 96$ °C) was measured on three different days (one in November 2019 and two in August 2020), with measurements taken at regular intervals from 09:30 to 17:00 (UTC +3) to record diurnal variations in H_2 activity. In November 2019, measurements were collected throughout the study site; accordingly, the measurement values for this period (*i.e.*, orange dots in Fig. 4) were obtained from slightly different locations. To consider conditions at depth, we discuss

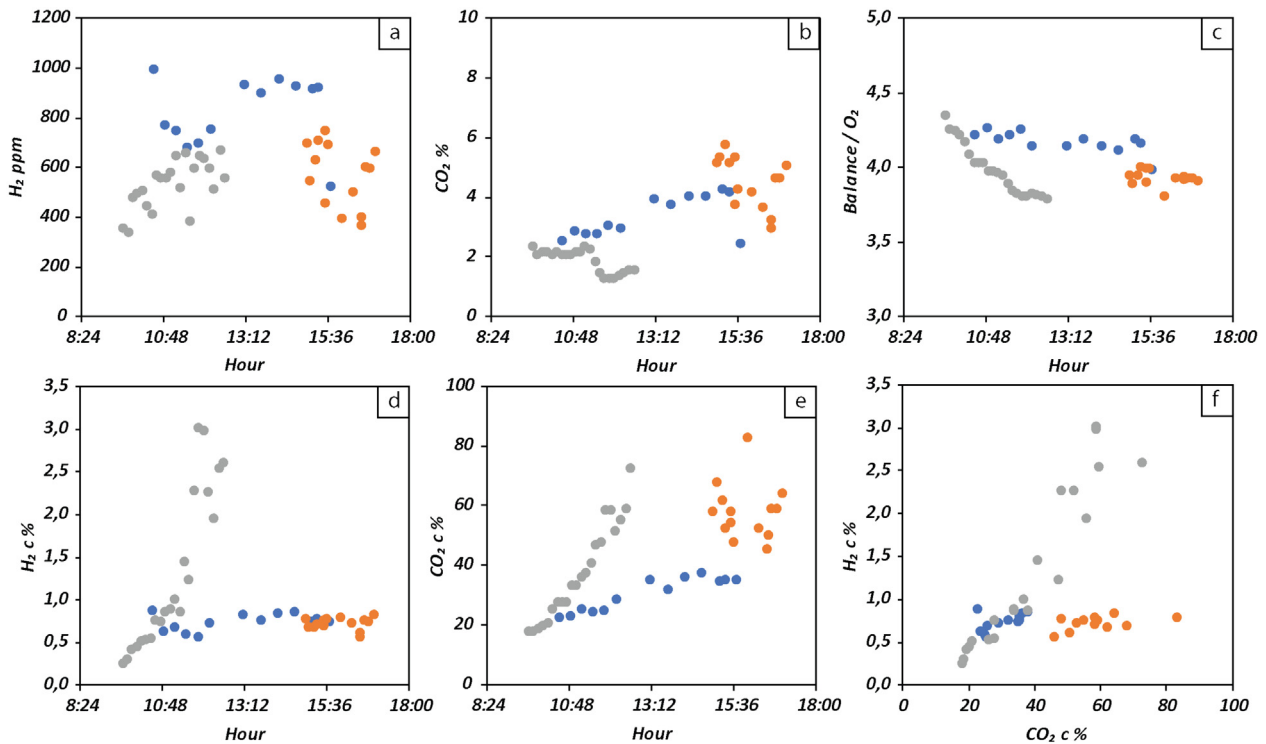


Fig. 4. Evolution of gas content with time for the fumaroles of Site 4 within the Asal–Ghoubbet rift. Orange points 21/11/2019; blue points 12/08/2020; gray points 13/08/2020. (a) H_2 (ppm) *in situ* as a function of time. (b) CO_2 (%) *in situ* as a function of time. (c) Balance/ O_2 as a function of time for air variation in the analysis. (d) Diurnal variation in H_2 , after correction. (e) Diurnal variation in CO_2 , after correction. (f) Corrected H_2 as a function of corrected CO_2 (Pasquet *et al.*, 2021).

here the results from drill cuttings obtained from the F1 and Glc1 geothermal wells; we collected 37 samples down to 1118 m and 10 samples down to 458 m for F1 and Glc1, respectively.

3.1 Gas emissions

Site 4 is an active hydrothermal site along the inner margins of the Asal–Ghoubbet rift, located to the southwest of the Fiale Caldera near wells F1 and A5 (Fig. 2). Fumaroles escape from a major rift fault with a gas temperature exceeding 96°C . This site has been shown to exhibit the highest surface H_2 concentrations in the area, with values exceeding 1000 ppm (Pasquet *et al.*, 2021). The temporal evolution of H_2 and CO_2 at this site is illustrated in Figure 4, with data points color coded according to sampling day.

For our uncorrected dataset, bell trends in *in situ* H_2 concentrations were observed, with the highest values (900–1000 ppm) were typically observed between 13:00 and 15:00 (Fig. 4a). In contrast, *in situ* CO_2 measurements increased with time to a maximum value of approximately 6% (Fig. 4b).

A major problem encountered in this region, as in many volcanic emissions, is that the sampled gas is a mixture of volcanic gas and atmospheric air. The volcanic gases can be diluted with air by the thermal contrast between the emanations and the atmospheric air, by the lava corridors formed during previous eruptions, or by the large faults in the vegetation-free landscape, which induce high vertical and horizontal permeability. The field analyzer measured CH_4 , CO_2 , O_2 ,

H_2 , CO , H_2S , and the balance. As already stated, a water filter was placed upstream of the analyzer to obtain the dry gas concentration; volcanic gas typically contains approximately 80% water vapor. Then, having measured the O_2 concentration and if the balance is considered to contain mostly N_2 (*i.e.*, if the balance/ O_2 ratio is higher than that of the atmosphere), the measured gas can be corrected. To do this, we subtracted the O_2 compound, which we considered to be outside the system, and removed the equivalent volume of N_2 from the balance according to the atmospheric ratio $N_{2(\text{atm})}/O_{2(\text{atm})}=3.727$. Similarly, argon was removed from the balance according to the ratio $Ar_{(\text{atm})}/O_{2(\text{atm})}=0.044$. We observed a temporal trend in the balance/ O_2 for samples taken on two days (*i.e.*, blue and orange points in Fig. 4c), which allowed us to make this correction. This ratio was higher than 3.7, indicating that the balance contains other gases than atmospheric N_2 (Ar, He, SO_2 ...). In contrast, a different temporal trend was observed for the other sampling day (*i.e.*, gray points in Fig. 4c): we observed a constant decrease of the balance/ O_2 ratio between 4.3% and 3.8%, associated with an increase in O_2 concentration from 18.2% to 20.5% (Fig. 4c).

Once these air corrections were made, H_2 concentration was found to remain relatively constant throughout the day for samples collected in November 2019 and on August 12th, 2020, with values between 0.57% and 0.89%. However, after correction, the H_2 concentrations obtained on August 13th, 2020 exhibited a strong positive diurnal trend, increasing from 0.31% to 3% over the course of the day (Fig. 4d). This could be explained by a higher concentration of O_2 , and so a bigger

correction on air (raw data are available in [Supplementary material 1](#)).

Our corrected CO₂ concentrations exhibit no notable trend for the samples collected in November 2019. Concentrations measured on August 12th, 2020 increased from 21% to 36% over the course of the day, while the strongest positive correlation was observed on August 13th, 2020 ([Fig. 4e](#)). Finally, we observed a positive correlation between H₂ and CO₂ ([Fig. 4f](#)), as shown previously by [Pasquet *et al.* \(2021\)](#).

3.2 Microbial taxonomic diversity

Following microbial analysis of soil samples collected at Site 4 in 2019, samples were collected in three different locations in 2021. DNA samples were extracted from these soils and the 16S rRNA genes were amplified and sequenced to taxonomically identify the prokaryotes present. The number of sequences analyzed (following high-throughput sequencing and the removal of low-quality reads and chimera) was as follows: 19,038, 15,467 and 17,338 sequences for Site 4 2019; 15,359, 17,993, and 18,144 sequences for Site 4 2021 (zone 13); 18,454, 19,663 and 18,368 sequences for Site 4 2021 (zone 15); and 17,614, 18,462 and 13,611 sequences for Site 4 2021 (zone 16). The analysis of these sequences indicated a very high dissimilarity between the communities collected in 2019 and 2021, as illustrated by the Heatmap ([Fig. 5](#)).

As shown in [Figure 6](#), the microbial community of 2019 included few archaea (>2%), while the 2021 community was dominated by these prokaryotes (with $91 \pm 13\%$ for Site 4 2021 [zone 13] and $93 \pm 3\%$ for Site 4 2021 [zone 15]). Site 4 2021 (zone 16) revealed another equilibrium between bacteria and archaea ($37 \pm 4\%$), which could be explained by the presence of abundant chloroplasts ($28 \pm 3\%$). The archaea belonged primarily to the phylum Crenarchaeota, including the classes Nitrososphaeria and Thermoprotei, and to the orders SCGC AB-179-E04 (from $33 \pm 4\%$ to $79 \pm 13\%$) and Geoarchaeles (from $4 \pm 0\%$ to $19 \pm 16\%$), respectively. No archaea similar to methanogens were identified at this site during either sampling campaign. In addition, enrichments carried out in the dark under anoxic and oxic conditions showed no significant consumption of H₂ or CO₂ present in the gas phase, during incubation carried out for 10 days.

Regarding bacteria, the community from Site 4 in 2019 included mainly the following orders: Kapabacteriales ($15 \pm 1\%$), Thermoflexales (family of *Thermoflexaceae*; $8 \pm 3\%$), Thermomicrobiales (*Thermomicrobiaceae*; $8 \pm 4\%$), Cyanobacteriales (*Nostocaceae*; $14 \pm 3\%$), Brevibacillales (*Brevibacillaceae*; $10 \pm 4\%$), Paenibacillales (*Paenibacillaceae*; $5 \pm 2\%$), and Symbiobacteriales (*Symbiobacteraceae*; $3 \pm 2\%$). The presence of organisms affiliated to the class of Hydrothermae ($14 \pm 3\%$) should also be noted. For the second sampling campaign, in zones 13 and 15, bacteria represented only 6–8% of the relative abundance of the communities present. Only the community at Site 4 2021 (16) exhibited a relatively high abundance, with 63% of bacteria belonging to the orders Pseudonocardiales (*Pseudonocardiaceae*; $7 \pm 1\%$), Ktedonobacteriales (*Ktedonobacteraceae*; $5 \pm 1\%$), and Gemmatales (*Gemmataceae*; $7 \pm 2\%$).

3.3 Bulk analysis

The total rock analyses performed by ICP–OES for the F1 and Glc1 wells ([Tab. 1](#)) demonstrate elemental variations with depth in the inner and outer margins. For the F1 well, SiO₂ concentrations remained relatively constant with depth, typically in the range 44–47%, although SiO₂ values closer to 50% were observed at a few depths. In contrast, sample 15 (304 m) was particularly poor in SiO₂ (31.86%). For Glc1, SiO₂ concentrations were more variable: typically, these were lower than 45% for the first 280 m and higher than 45% in the rest of the cuttings, reaching up to 66% for sample 10 (458 m).

A transition is apparent in well F1 at 464 m depth ([Fig. 7](#)). Al₂O₃ concentrations were higher at depths of 0–464 m, typically varying between 18.86 and 25.32%, compared to 11.95–21.21% in the rest of the well. Most other parameters analyzed generally exhibited lower values at shallower depths (*i.e.*, 0–464 m), including total iron (4.45 to 8.81%), TiO₂ (0.67 to 1.47%), Na₂O + K₂O (2.18 to 2.46%), and loss on ignition (LOI; 1.31 to 5.69). However, concentrations of CaO were higher at these depths (12.18 to 15.39%) than elsewhere. Values at 518–1118 m were as follows: 5.51–15.83% for Fe₂O₃; 0.97–3.48% for TiO₂; 2.67–6.20% for Na₂O + K₂O; 2.07–9.37% for LOI; and 5.12–13.54% for CaO.

In well Glc1, a transition was also observed at 280 m depth ([Fig. 7](#)), with lower SiO₂ contents and higher Fe₂O₃, MgO, CaO, and TiO₂ contents at depths of 0–280 m relative to the rest of the well. In contrast, Al₂O₃ contents remained relatively constant with depth ($\sim 13 \pm 1.5\%$).

A global decrease in LOI with depth was found for well Glc1, whereas LOI was found to increase slightly with depth in well F1. In both wells, Fe₂O₃ peaks were associated with TiO₂ peaks (*e.g.*, at 250 m and 280 m for Glc1; at 616 m, 894 m, 954 m, and 1016 m for F1).

Sample 15 from well F1 is totally different from the surrounding basalts, with SiO₂, CaO, and LOI values of 31.86%, 30.28%, and 25.87%, respectively.

On a total alkali–silica (TAS) diagram ([Fig. 8](#)), the F1 well cuttings are concentrated in the area of basalts with relatively homogeneous SiO₂ concentrations ($44\% < \text{SiO}_2 < 47\%$). However, some of the samples exhibited higher silica concentrations and could be described as hawaiite-type trachybasalts or andesitic basalts ($\text{SiO}_2 > 50\%$). All of the basalts are distributed close to the straight line separating alkaline basalts from tholeiitic basalts, with samples from proximal levels in the tholeiitic domain and the deeper samples in the alkaline domain. A few samples exhibited SiO₂ concentrations below 45%, placing them closer to picrobasalts and basanites, which are more basic and richer in normative olivine.

The data from the Glc1 well cuttings are more heterogeneous, despite remaining predominantly within the basaltic domain. Samples from shallower levels tend towards alkaline basalts, whereas those from deeper levels are typically tholeiitic basalts. However, point 10, from 548 m, is particularly rich in SiO₂ (66%) and is therefore more acidic and located within the dacite zone.

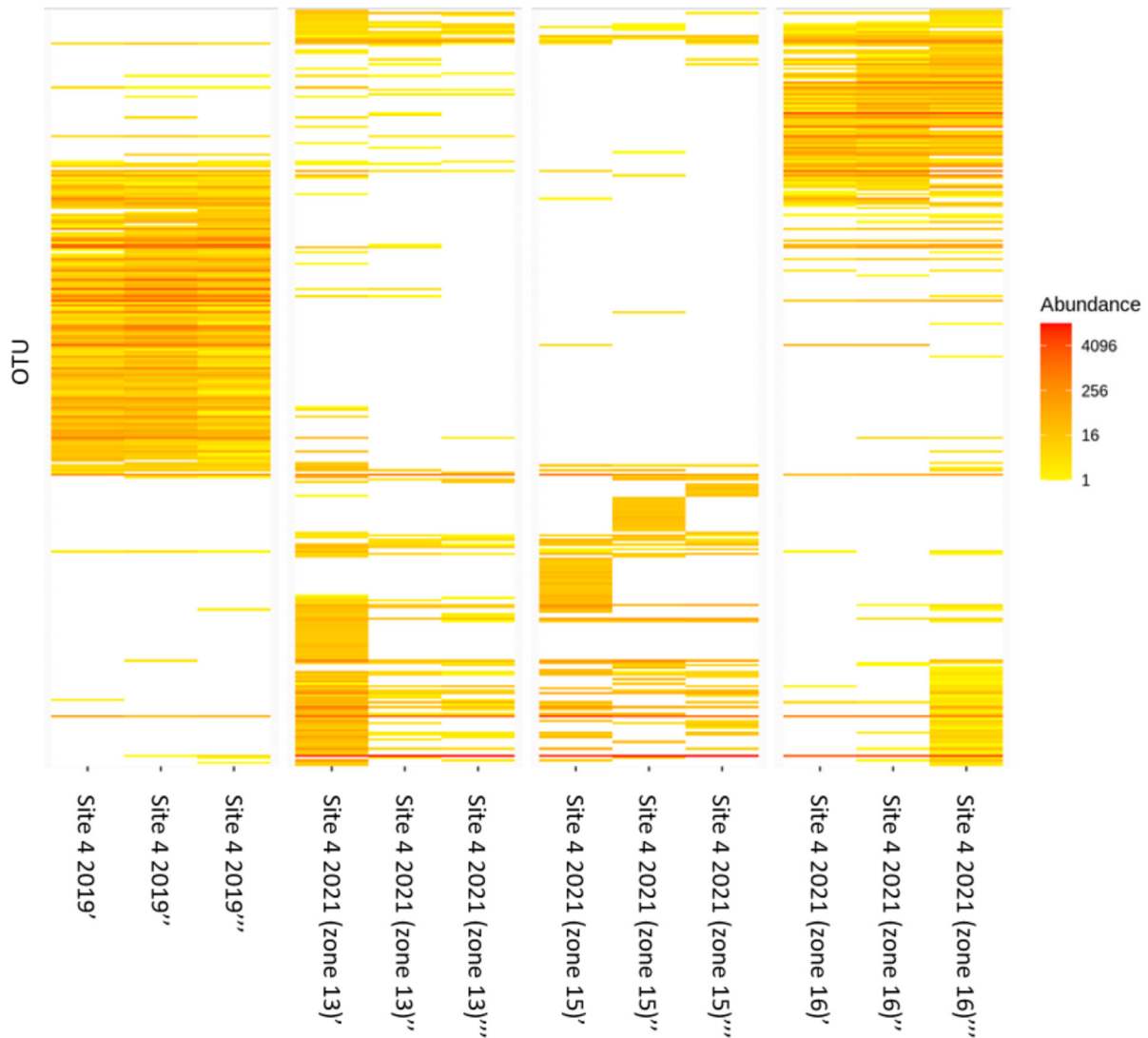


Fig. 5. Heat map showing the distribution of 326 microbial OTUs (Operational Taxonomic Units) at Site 4 based on two sampling campaigns (2019 and 2021 for zones 13, 15 and 16). High-throughput sequencing was performed using 16S rRNA gene amplicon (v3–v4).

3.4 XRD analysis

In addition to the major primary minerals, such as plagioclase (mainly labradorite and bytownite), clinopyroxene (solid solution between diopside and augite), the XRD analyses revealed the appearance at depth of secondary minerals (Fig. 9). Some minerals, such as olivine or zeolites, which are present in low amounts, were difficult to detect due to poor because the signal-over-noise ratio is too low to distinguish their weak concentrations. In addition, many peaks overlap each other.

In well F1 (37 samples; XRD patterns in [Supplementary material](#)), the secondary minerals found include smectite at 208 m and calcite at 464 m; quartz was detected in sample 21 at 518 m, chlorite at 536 m, and epidote at 854 m. Pyrite began to appear at 694 m, although in very low concentrations. Magnetite-rich sections were found between 518 m and 616 m depth and from 894 m to 1118 m. Zeolites were very rare.

In well Glc1 (10 samples; XRD profiles in [Supplementary material](#)), kaolinite, calcite and quartz are present in the samples extracted from the top of the well. No secondary minerals were observed between 250 and 280 m. Analcime zeolites were observed in the first 160 m of the well, whereas smectite began to appear below 280 m. Secondary minerals typical of higher temperatures, such as chlorite, epidote, and pyrite, were not detected by XRD.

3.5 Mössbauer spectroscopy analysis

^{57}Fe Mössbauer analyses were performed on 20 samples from well F1 and 10 samples from well Glc1 (Tab. 2). These data allowed the $\text{Fe}^{2+}/\text{Fe}^{3+}$ ratios in the rocks to be determined and allowed iron-bearing minerals to be identified. The main minerals found were ferrihydrite ($\text{Fe}^{3+}_5\text{HO}_8 \cdot 4\text{H}_2\text{O}$), clinopyroxene ($(\text{Ca}, \text{Na}, \text{Mg}, \text{Fe}^{2+}, \text{Al}, \text{Ti})_2(\text{Si}, \text{Al})_2\text{O}_6$), olivine ($(\text{Fe}^{2+}, \text{Mg})_2\text{SiO}_4$), ilmenite ($\text{Fe}^{2+}\text{TiO}_3$), hematite ($\text{Fe}^{3+}_2\text{O}_3$), magnetite ($\text{Fe}^{2+}\text{O} \cdot \text{Fe}^{3+}_2\text{O}_3$), and maghemite ($\gamma\text{-Fe}^{3+}_2\text{O}_3$) in the first

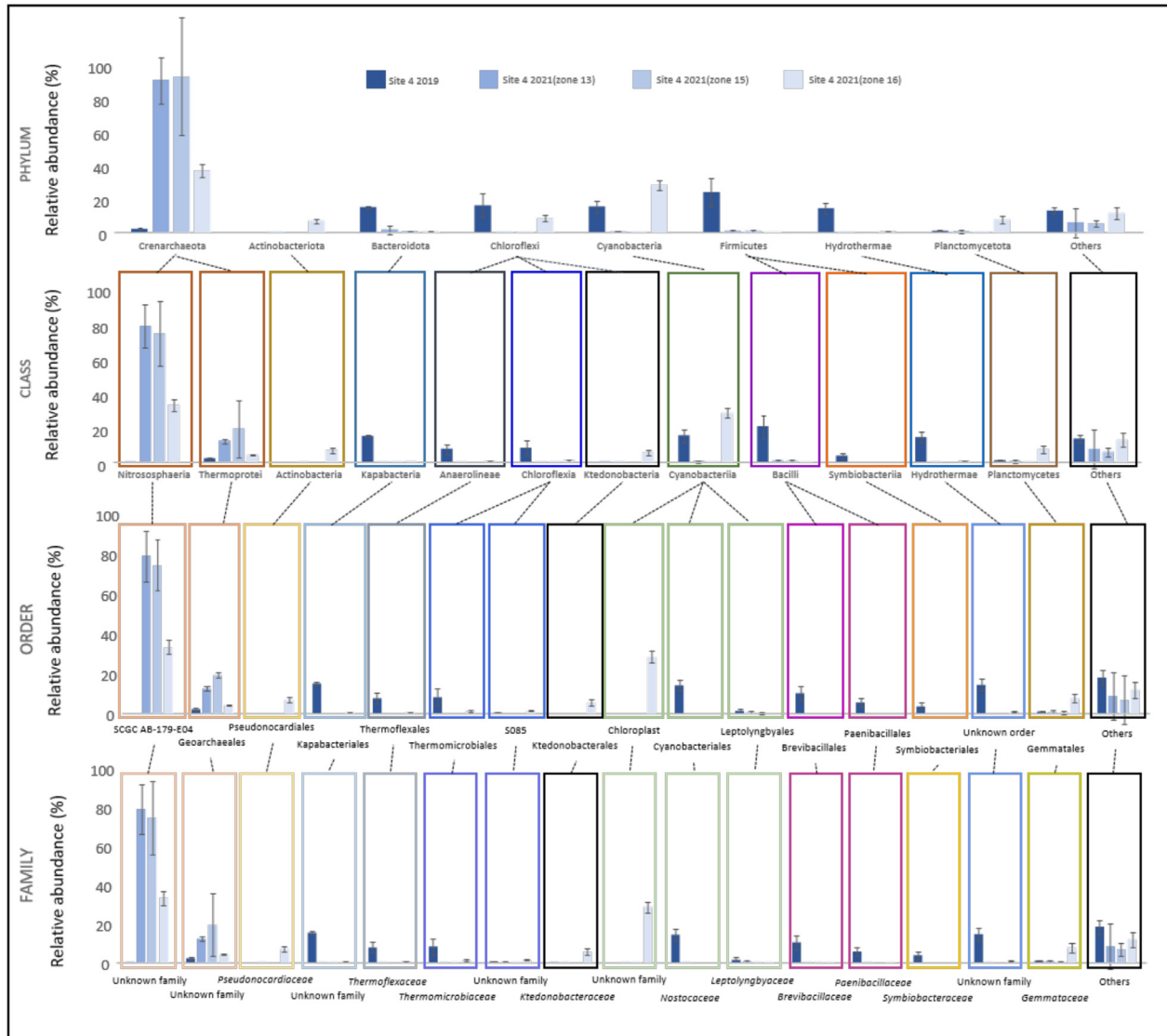


Fig. 6. Representation of the taxonomic diversity of microbial communities at Site 4 during the two sampling campaigns (and for several zones, in the case of the 2021 campaign). High-throughput sequencing was performed using 16S rRNA gene amplicon (v3–v4).

part of the well (*i.e.*, depths up to 464 m). At greater depths, a Fe-rich chlorite like chamosite (iron end-member of chlorite: $(Al, Fe^{2+}, Fe^{3+}, Mg)_6(Si_3Al)O_{10}(OH)_8$) was found in place of olivine and maghemite disappeared (Tab. 2).

The phase mixtures in these rocks are quite complex and the Mössbauer spectra exhibit various components (quadrupole doublets and magnetic sextets) associated with different Fe-bearing minerals. The analyses were carried out at room temperature; accordingly, there is some uncertainty in the attribution of some components. Indeed, the Fe^{3+} doublets characterized by isomer shift (δ) values ranging from 0.35 to 0.38 mm/s and rather large quadrupole splitting ($0.60 \leq \Delta \leq 0.84$ mm/s) could correspond to either ferrihydrite or Fe^{3+} -chlorite (Fig. 10). Moreover, this component often exhibits broad resonance lines ($\Gamma > 0.60$ mm/s) that could hide a low-intensity doublet associated with pyrite ($Fe^{2+}S_2$) which is characterized by $\delta \approx 0.30$ mm/s and $\Delta \approx 0.5$ mm/s. Similarly,

the ^{57}Fe Mössbauer hyperfine parameters of the Fe^{2+} doublets due to olivine and Fe^{2+} -chlorite are very similar. Further analysis at different temperatures would allow these Fe^{3+} or Fe^{2+} -bearing phases to be distinguished. This study has taken the approach of interpreting these doublets and sextets considering the results of XRD analyses and especially, the detection of chlorite XRD pattern in the diffractograms. Thus, the concentration of chlorite is likely to be overestimated in comparison with olivine and the proportion of pyrite likely underestimated.

Fe^{3+} was found to be carried by ferrihydrite, maghemite, and hematite at depths of 0–464 m but primarily by Fe-rich chlorite and magnetite at greater depths (Tab. 2). An additional threshold was observed at 518 m, where ferrihydrite, maghemite, and Fe-clinopyroxene were replaced by Fe-chlorite. Despite the highest concentrations of Fe_{total} being observed below 464 m depth, the percentage of Fe^{3+} in the

Table 1. Chemical compositions of Fiale 1 and Glc1 cuttings in Ox%.

Sample	Depth	Temp.	SiO ₂	Al ₂ O ₃	Fe ₂ O ₃ *	MnO	MgO	CaO	Na ₂ O	K ₂ O	TiO ₂	P ₂ O ₅	LOI	Total
D4-1	0	95	38.79	23.91	11.57	0.17	2.94	1.61	0.10	0.05	2.45	0.26	17.60	99.44
D4-13	0	95	46.61	23.28	6.41	0.10	3.55	14.47	1.96	0.17	1.30	0.16	1.48	99.51
<i>Fiale 1</i>														
12	149	32	46.43	22.94	7.09	0.091	3.78	14.52	2.01	0.17	1.47	0.15	1.31	99.95
13	208	32	46.12	22.45	7.17	0.096	4.73	13.99	2.04	0.21	1.14	0.13	1.79	99.84
14	254	35	46.03	19.89	8.32	0.12	5.97	13.04	2.22	0.23	1.43	0.18	2.27	99.70
15	304	47	31.86	4.19	4.49	0.065	1.23	30.28	0.50	0.20	0.36	0.13	25.87	99.17
16	354	85	44.69	18.86	8.81	0.12	4.94	12.18	2.29	0.31	1.57	0.22	5.69	99.68
17	404	145	44.18	23.84	5.47	0.10	3.21	14.86	2.01	0.22	1.08	0.00	4.46	99.42
18	437	160	44.76	23.44	5.68	0.090	4.17	14.25	2.02	0.22	1.01	0.00	3.72	99.35
19	464	168	44.63	25.32	4.45	0.083	2.81	15.39	1.83	0.57	0.67	0.00	3.71	99.46
21	518	190	44.66	18.78	9.65	0.14	3.96	11.16	2.65	0.81	1.63	0.22	5.94	99.59
22	536	195	43.73	17.85	8.52	0.14	3.91	13.54	2.36	0.41	1.42	0.20	7.94	100.02
23	552	200	44.78	17.36	10.20	0.17	3.70	10.24	2.73	0.75	2.13	0.37	6.54	98.96
24	574	205	50.77	13.50	10.11	0.21	4.15	5.36	2.41	3.44	2.34	0.42	6.65	99.36
25	592	205	47.66	15.57	10.23	0.22	3.78	8.71	2.37	2.10	2.03	0.33	6.21	99.21
26	616	207	47.02	12.75	15.83	0.28	4.59	8.17	3.39	0.63	3.48	0.51	2.07	98.73
27	634	207	46.13	17.74	9.85	0.20	5.02	7.55	3.16	1.80	2.27	0.53	5.29	99.53
28	654	208	46.58	16.19	10.84	0.21	5.19	6.48	2.96	1.79	2.38	0.45	6.50	99.57
29	674	209	45.13	18.88	8.06	0.21	3.65	9.87	3.18	1.53	1.53	0.23	6.64	98.94
30	694	210	46.82	14.23	12.33	0.16	4.91	5.12	2.46	2.48	2.43	0.37	7.82	99.14
31	714	205	51.20	18.19	6.98	0.13	3.32	7.35	2.04	4.16	1.29	0.20	4.80	99.64
32	734	190	44.94	14.07	11.66	0.29	5.12	8.55	3.26	0.67	2.34	0.32	7.80	99.03
33	754	180	46.62	17.36	7.45	0.19	3.85	10.56	3.35	1.17	1.38	0.19	7.07	99.18
34	774	170	47.19	21.21	5.51	0.13	3.39	10.82	3.74	0.93	0.97	0.14	5.91	99.93
35	794	162	44.76	18.14	8.54	0.17	4.26	10.73	3.41	0.77	1.60	0.22	6.60	99.20
37	838	150	47.22	17.22	9.34	0.19	4.27	8.56	3.16	1.20	1.84	0.29	6.04	99.33
38	854	145	45.73	11.91	10.41	0.20	3.72	11.26	3.32	0.90	2.11	0.37	9.37	99.29
39	871	135	44.66	17.52	8.10	0.19	2.64	11.64	3.06	1.85	1.55	0.24	7.99	99.43
40	894	127	46.27	14.93	12.82	0.23	5.09	10.34	3.08	0.35	2.64	0.37	3.38	99.51
41	914	120	47.61	15.64	9.97	0.23	3.92	9.29	3.65	0.62	1.85	0.32	6.37	99.47
42	934	115	52.44	11.95	8.87	0.19	3.25	9.73	3.05	0.19	1.67	0.35	7.57	99.26
43	954	110	45.58	13.35	13.37	0.23	5.17	10.82	2.49	0.18	2.70	0.39	4.89	99.16
44	974	107	45.54	18.89	9.60	0.17	3.96	11.94	2.76	0.11	2.02	0.23	4.43	99.64
45	994	100	44.94	18.15	9.37	0.16	4.62	12.01	2.54	0.12	1.72	0.20	5.93	99.76
46	1016	95	45.83	14.45	12.55	0.20	5.93	12.24	2.50	0.19	2.61	0.35	2.43	99.28
47	1034	92	47.49	18.86	9.04	0.16	4.52	12.34	3.13	0.13	1.61	0.21	2.82	100.29
48	1054	90	47.16	16.09	9.68	0.16	3.54	10.28	3.63	0.17	1.99	0.33	6.09	99.12
50	1091	85	46.24	19.30	9.29	0.17	4.10	12.08	3.03	0.32	1.78	0.23	2.93	99.46
51	1118	77	45.58	17.75	8.33	0.17	3.45	13.07	2.78	0.10	1.77	0.23	6.90	100.14
<i>Glc 1</i>														
1	76	35	36.75	11.29	11.26	0.16	4.08	12.52	2.07	0.78	2.33	0.48	17.88	99.60
2	160	50	38.09	14.41	8.34	0.15	5.01	10.12	1.84	0.68	1.54	0.28	18.75	99.21
3	250	90	43.37	13.38	14.52	0.22	4.97	10.83	2.73	1.10	3.06	0.53	4.34	99.06
4	280	110	42.90	14.57	13.66	0.22	6.49	11.01	2.61	0.41	2.67	0.36	4.68	99.58
5	310	115	49.68	13.06	9.22	0.24	3.19	4.82	1.87	2.25	1.38	0.27	14.08	100.06
6	340	120	48.65	13.12	9.42	0.19	3.19	5.51	1.18	1.60	1.45	0.34	14.89	99.54
7	370	125	45.98	14.57	9.65	0.20	4.31	8.61	2.45	1.16	1.56	0.29	10.92	99.69
8	400	130	51.81	13.90	9.85	0.14	3.86	4.30	1.59	3.36	1.28	0.30	9.85	100.22
9	420	130	50.20	12.50	8.09	0.15	3.23	8.18	1.66	3.07	1.08	0.26	11.98	100.39
10	458	130	66.50	10.53	4.56	0.12	1.73	4.48	0.88	3.28	0.59	0.11	7.59	100.36

Samples D4-1 and D4-13 are from [Pasquet *et al.* \(2021\)](#). Fe₂O₃* is for total iron.

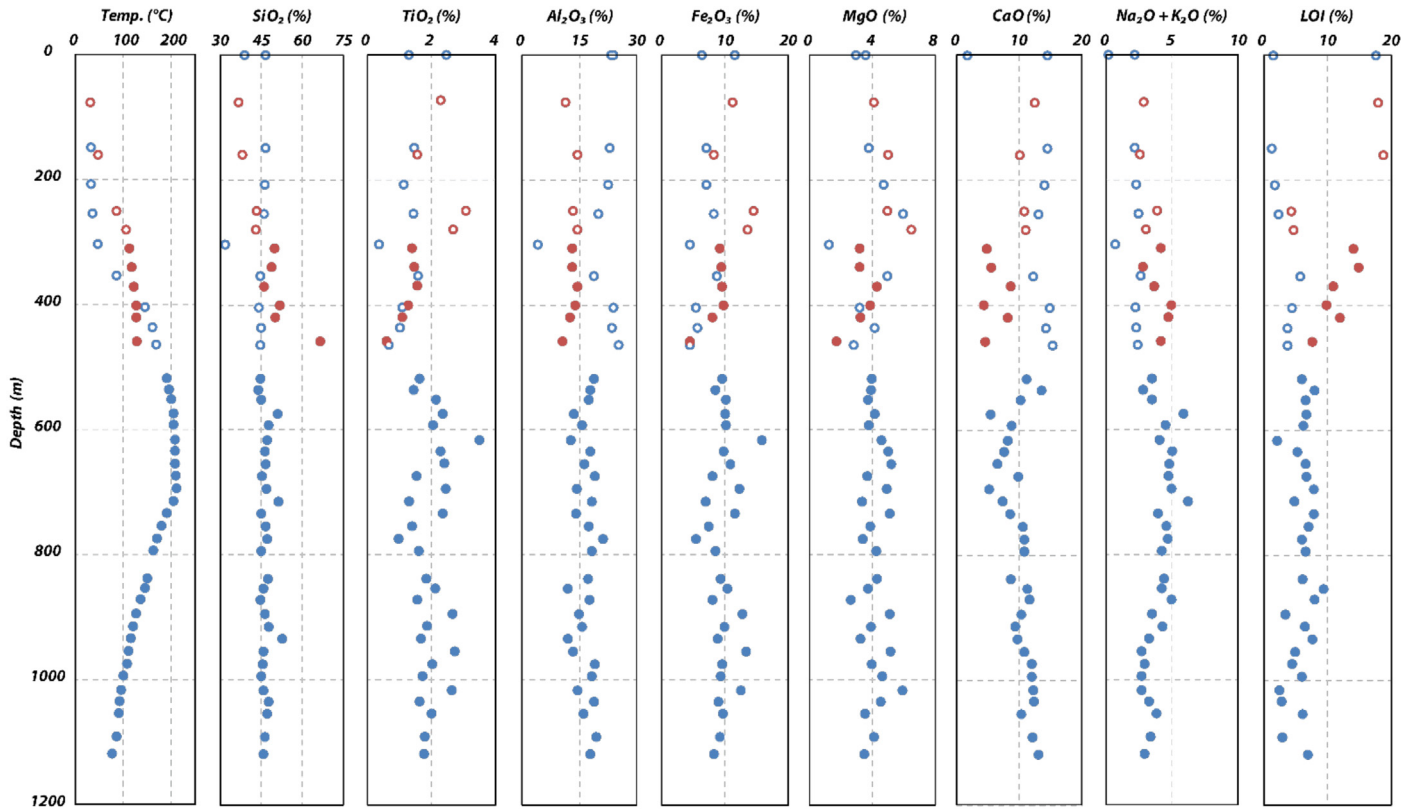


Fig. 7. Chemical evolution (Ox%) with depth for the cuttings from the Fiale 1 (blue dots) and Gale le Goma 1 (red dots) wells. Asal series samples are represented by empty circles and Stratoïd series by solid circles.

rock was significantly lower (24–55%) at greater depths than at depths less than 464 m (63–77%; Fig. 11).

4 Discussion

Here, we discuss how our results allow us to better define the dihydrogen system of the Asal–Ghoubbet rift; this includes inferring the H_2 source rock, migration pathways, reservoir rock, and a seal in the Fiale area.

4.1 Well lithologies

We produced simplified lithological logs (Fig. 12) by comparing our XRD and bulk rock analysis results; the resolution of these logs is based on the spacing of the well cuttings, *i.e.* 20–50 m for F1 and 20–90 m for Glc1. Unsurprisingly, the rocks in these two wells are mainly basalts. These basalts are transitional, essentially composed of plagioclase (solid solution between labradorite and bytownite) and clinopyroxene (solid solution between diopside and augite). They can be divided into two domains: basalt with a tholeiitic tendency (0–464 m for F1) and basalt with an alkaline tendency (464–1118 m for F1) (Figs. 7 and 8). The first domain corresponds to the basalts of the Asal Series (1 Ma to present) and the second to the Afar Stratoïd Series (4–1 Ma). The basalts of the Asal Series are richer in plagioclase so richer in CaO%.

The transition between the two series, although marked in both wells, is less pronounced in well Glc1. Indeed, the

composition of the lavas here are known to have varied with time, with the basalts of the Asal Series along the external rift margins exhibiting compositions that are more intermediate than tholeiitic (Stieltjes *et al.*, 1976). In our dataset, the transition from the basalts of the Asal Series to the Stratoïd Series was observed to occur at 280 m. The Asal Series is thicker along the rift axis.

Basalts with a Fe_2O_3 (total iron) composition above 15% (Ox%) are considered to be ferrobasalts (Stieltjes *et al.*, 1976) and are associated with high TiO_2 concentrations (>3.48%) (Tab. 1). Many of these basalts are rich in iron (>10%) and titanium (>2%) but cannot be classed as ferrobasalts because their Fe_2O_3 content is lower than 15%. This correlation suggests high levels of ilmenite and titanomagnetite ($Fe^{2+}(Fe^{3+},Ti)_2O_4$). SiO_2 peaks are often correlated with $Na_2O + K_2O$ peaks, corresponding to more acidic rocks such as andesite basalts or trachybasalts.

LOI can be used as a proxy for the alteration rate of basalts; here, many samples exceeded 5%, which indicates argillization/chloritization of the rock. At shallow depths in well Glc1 (160–200 m), LOI values above 15% are considered to indicate hyaloclastites, which were formed under seawater. Conversely, the first cuttings from well F1 (*i.e.*, from depths up to 250 m) exhibited LOI values lower than 2.5%. These basalts can be considered unaltered or slightly altered; the XRD data support this interpretation, with less pronounced clay signals.

Finally, a sedimentary layer was observed at 300 m depth in F1; this layer was composed primarily of calcium carbonates

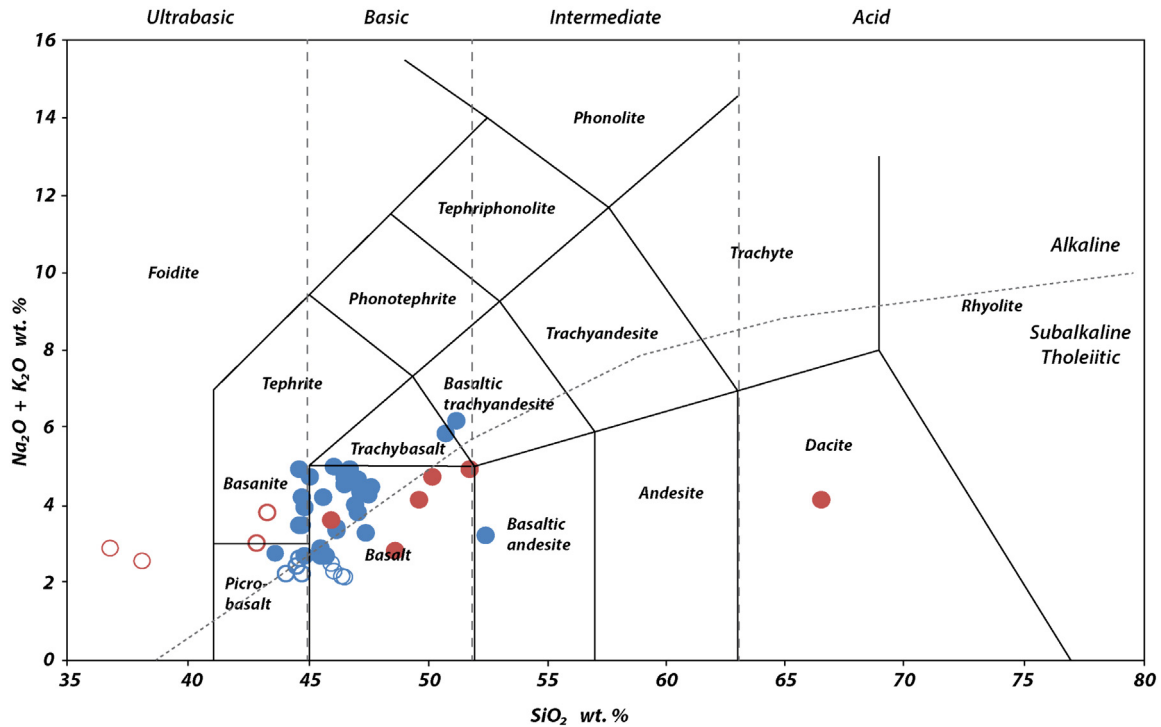


Fig. 8. TAS diagram representing the compositions of F1 (blue dots) and Glc1 (red dots) cuttings. Asal series samples are represented by empty circles and Stratoid series by solid circles.

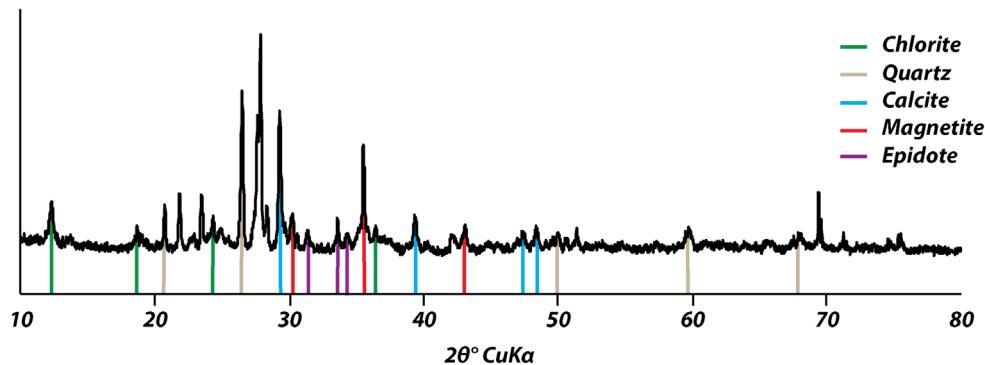


Fig. 9. Example of one of the XRD interpretations of secondary minerals on the F1-51 cuttings (1118 m depth). Ordinate in number of counts and abscissa in $2\theta^\circ$. Primary minerals peaks are not shown.

and quartz. Thus, the high Fe^{3+} concentration in the hyaloclastites at the margins indicates almost complete oxidation of the submarine basalts, in contrast to the open-air conditions along the axis. The underlying Stratoid Basalts, richer in total iron and also more altered, indicate a reconcentration of iron after alteration.

4.2 Secondary mineral occurrence

Secondary minerals provide information about the alteration degree of the basalts and the physicochemical conditions at depth. Based on our knowledge of conditions and the mineral phases present, it is possible to consider potential

redox reactions leading to H_2 formation and to determine whether a rock has already produced or could produce H_2 .

For well F1 (axial zone), temperatures reach a maximum of 210°C at 694 m depth, and 130°C at 400 m for Glc1 (external margins). Then, in the axial zone, temperature decreases from this 210°C maximum to approximately 60°C (see Tab. 1) owing to marine water intrusion (Zan *et al.*, 1990; Varet, 2014).

For well F1, we observed the successive appearance of smectites, calcite, quartz, chlorite, and then epidote with increasing temperature (Fig. 13); this is similar to the characteristics of well A5 as described previously (Zan *et al.*, 1990). Indeed, these minerals can be utilized to define temperature domains according to their dominance (Franzson *et al.*, 2008): 50 to 200°C for smectite–zeolites; 220°C to

Table 2. Distribution of iron content in mineral phases after Mössbauer spectroscopic analysis of F1 (12 to 51) and G1c1 (1 to 10) cuttings.

Sample	Depth (m)	Cpx (Fe ²⁺)	Frh (Fe ³⁺)	Olivine (Fe ²⁺)	Fe-Chlorite (Fe ³⁺)	Hematite (Fe ³⁺)	Magnetite (Fe ^{2+/3+})	Ilmenite (Fe ²⁺)	Magnetite (Fe ³⁺)	Pyrite (Fe ²⁺)	Fe ³⁺ /Fe _{total} (%)
12	149	31	24	3	—	14	6	—	16	—	63.0
13	208	24	22	—	—	20	3	—	28	—	74.5
14	254	26	23	3	—	8	5	4	30	—	68.5
16	354	28	26	8	—	8	12	8	12	—	64.0
17	404	14	36	11	—	6	6	8	13	—	64.0
18	434	15	31	9	—	16	6	3	14	—	70.0
19	464	4	26	11	—	15	8	4	24	—	77.0
21	518	10	16	12	—	20	11	2	18	—	68.5
22	536	—	—	—	18	31	9	—	—	—	62.5
23	552	—	—	—	20	13	8	3	—	—	45.0
26	616	17	—	—	16	7	16	14	—	—	47.5
30	694	—	—	18	37	—	—	—	—	17	37.0
33	754	—	—	—	17	21	7	3	—	—	48.5
38	854	—	—	—	12	28	5	—	—	—	55.5
39	871	—	—	—	20	7	5	4	—	—	34.5
43	954	11	—	—	14	6	14	10	—	—	41.5
47	1034	27	—	—	19	—	12	—	—	—	38.0
48	1054	—	—	—	11	8	13	6	—	—	38.5
50	1091	17	—	—	15	3	9	9	—	—	31.5
51	1118	—	—	—	11	—	9	8	—	—	24.0
1	76	4	80	—	—	—	2	12	—	—	95.0
2	160	—	78	—	—	22	—	—	—	—	100.0
3	250	19	25	—	—	20	3	30	—	—	79.5
4	280	24	19	—	—	23	5	24	—	—	73.5
5	310	—	76	4	—	20	—	—	—	—	96.0
6	340	—	44	56	—	—	—	—	—	—	44.0
7	370	19	36	30	—	—	4	—	7	—	42.0
8	400	—	39	26	—	35	—	—	—	—	74.0
9	420	—	35	17	—	48	—	—	—	—	83.0
10	458	—	47	19	—	19	—	—	—	—	66.0

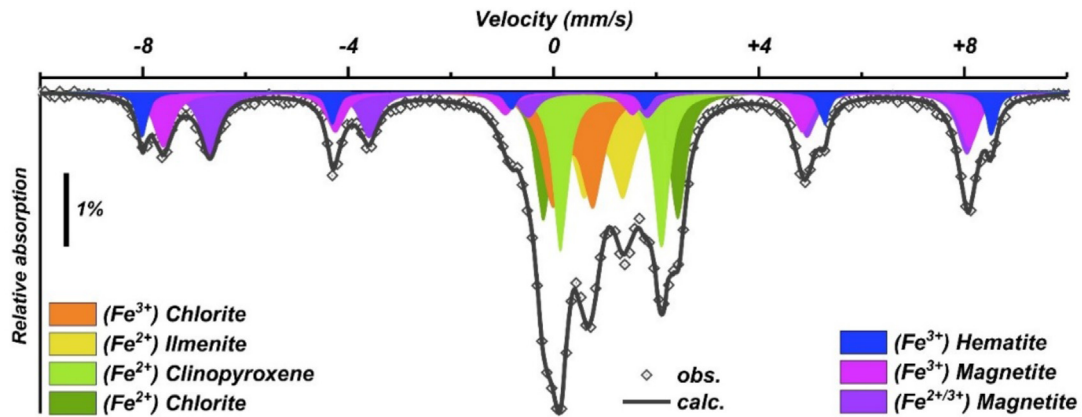


Fig. 10. Example of ^{57}Fe Mössbauer spectrum analysis (F1-26 sample).

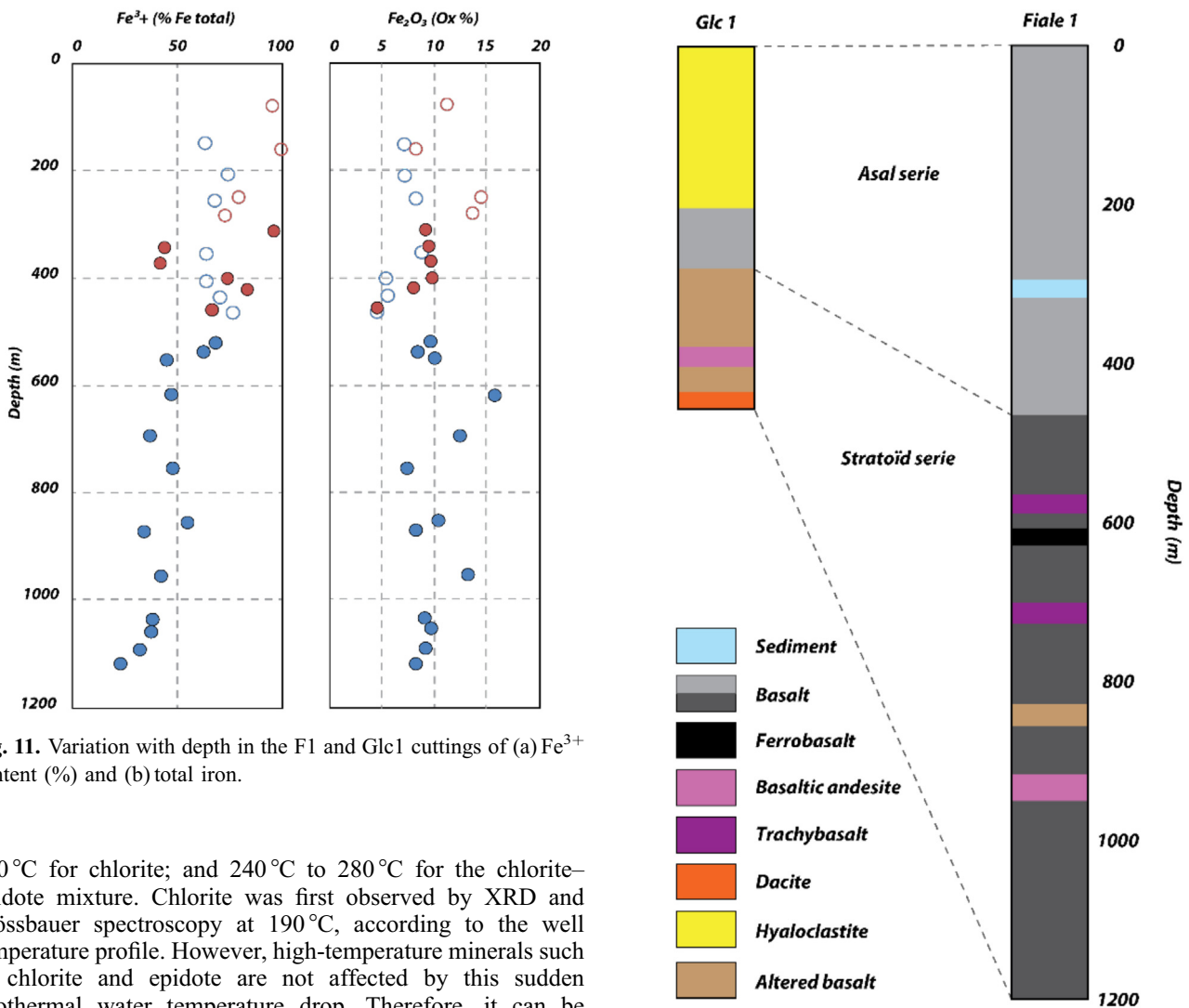


Fig. 11. Variation with depth in the F1 and Glc1 cuttings of (a) Fe^{3+} content (%) and (b) total iron.

240 °C for chlorite; and 240 °C to 280 °C for the chlorite–epidote mixture. Chlorite was first observed by XRD and Mössbauer spectroscopy at 190 °C, according to the well temperature profile. However, high-temperature minerals such as chlorite and epidote are not affected by this sudden geothermal water temperature drop. Therefore, it can be inferred that the secondary minerals are not currently in equilibrium with the fluid.

Fig. 12. Simplified lithological log of wells F1 and Glc1 from total rock and XRD analyses.

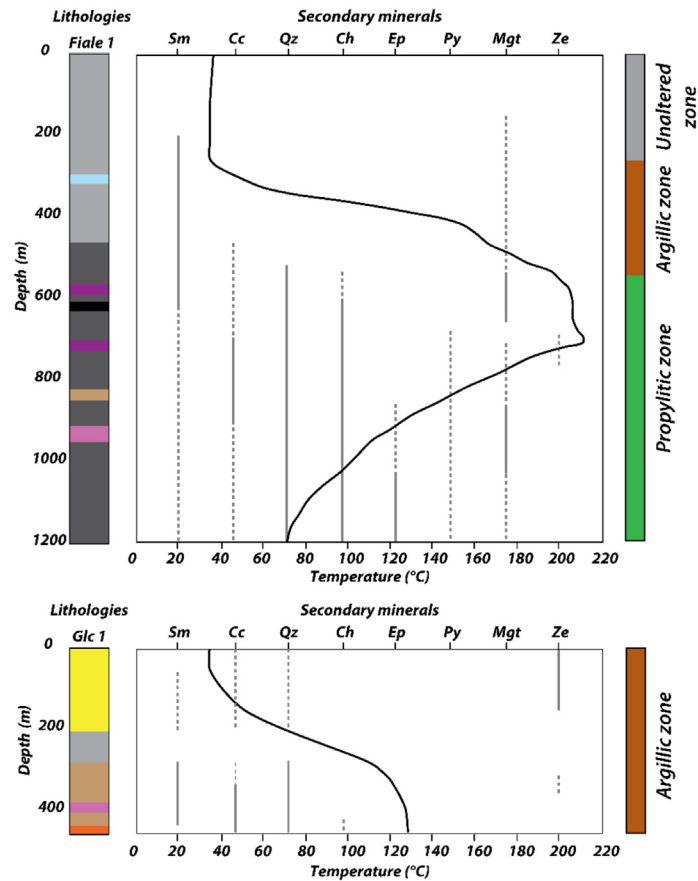


Fig. 13. Depth variation of secondary minerals in F1 and Glc1 wells from XRD and Mössbauer data (dashed lines) and temperature change with depth in the well (black line). Secondary minerals: Sm: smectite; Cc: calcite; Qz: quartz; Ch: chlorite; Ep: epidote; Py: pyrite; Mgt: magnetite; Ze: zeolite.

Secondary magnetite is a good proxy for H_2 production, but we assume that the titanomagnetite is principally of primary origin here, because there is a strong and uniform positive correlation between TiO_2 and Fe_2O_3 (Total) in our data (Fig. 14). Little pyrite was found in our samples. For well Glc1, a clear zeolite layer is evident in the first 160 m of depth. Deeper than 310 m, smectite and mixed-clay layers start to appear.

When considering H_2 production, both the observation of these alteration minerals and the alteration ratio are key to constraining potential cap rocks at depth. Despite the presence of a clay-rich layer around 850 m in well F1, it has not been possible to confirm that this layer is a good seal based on the LOI values (Tab. 1 and Fig. 7). However, at the external margin of the rift in well Glc1, fully weathered layers were observed over almost the first 400 m of depth; despite the presence of some unweathered layers, these locations may represent a suitable cap rock.

4.3 H_2 production

As already stated, continuous H_2 flow has been measured at the surface next to the Fiale Caldera, and some H_2 content has been detected in wells F1 and A5. The relative H_2 concentrations have been found to be 0.57–0.89% of the dry gas phase. This concentration is higher than that measured

at depth in well A3 (0.25% of the dry gas phase) and also higher than a purely volcanic degassing such as that during the Ardoukoba eruption in 1978 (0.145% of the dry gas phase; Allard *et al.*, 1979). After the volcanic degassing, this surface fumarolic H_2 may have been enriched by other processes, including redox reactions between iron-rich mineral phases and other liquid or gaseous phases.

Microbial communities in continuous H_2 flow have been studied in order to characterize their *in situ* taxonomic diversity and their potential to use H_2 as a source of energy and electrons from enrichment cultures. Indeed, it is known that microbial ecosystems can be hydrogen-based (Stevens and McKinley, 1995) with sulfate, carbon, dioxide or oxygen, for example, as acceptor electron. Given the environmental conditions at this site, in particular the high temperatures, our study of taxonomic diversity unsurprisingly revealed the presence of microorganisms known to be extremophiles; this includes the archaea, which are very well represented but not very diversified at this location. All of the archaea identified belong to the orders SCGC AB 179 E04 and Geoarchaeales, which have been described in thermal springs in the US (Havig and Hamilton, 2019). Similarly, the bacteria identified also belong to taxonomic groups already known to populate hot springs, such as the *Pseudonocardia* (Ningsih *et al.*, 2019), Kapabacteriales (Guajardo-Leiva *et al.*, 2021), *Thermoflexaceae* (Dodsworth *et al.*, 2014), *Thermomicrobiaceae*

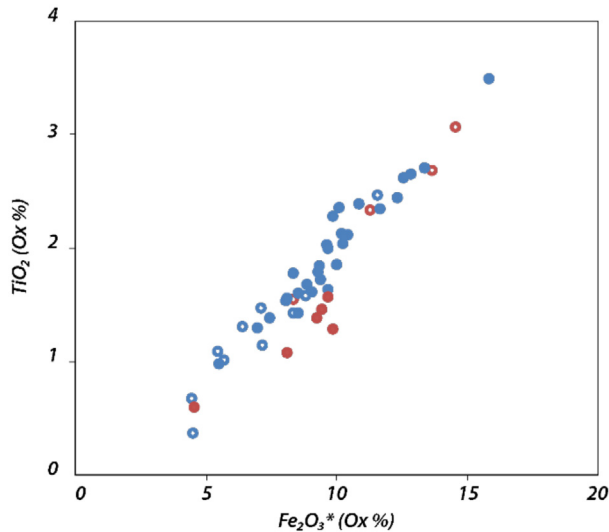
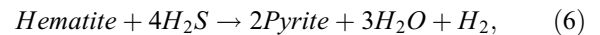


Fig. 14. Evolution of TiO_2 as a function of total iron in the cuttings of F1 and Glc1.

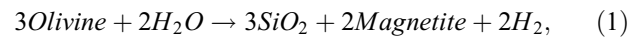
(Al Saade *et al.*, 2022), *Ktedonobacteraceae* (Arif *et al.*, 2021), *Nostocaceae* (Ansary *et al.*, 2017), *Brevibacillaceae* (Inan *et al.*, 2016), *Paenibacillaceae* (Panosyan *et al.*, 2020), and Hydrothermae (Smrhova *et al.*, 2022). Much affiliation remains vague at the order or even class level, since hot springs are extreme environments from which few microorganisms can be cultured and studied (López-López *et al.*, 2013; Marín-Paredes *et al.*, 2021); this justifies the need to multiply the studies of these extreme environments. In order to better understand them. Our results illustrate variation in taxonomic diversity both spatially (*i.e.*, between Site 4 2021 [zone 13], Site 4 2021 [zone 15], and Site 4 2021 [zone 16]) and, particularly, temporally (*i.e.*, between 2019 and 2021). This seems to suggest that unstable environmental conditions are strongly influencing the structuring of communities. Most of the microorganisms identified are aerobic and the presence of cyanobacteria and chloroplasts (algae) suggest the influence of oxygenic photosynthesis as a key metabolism of two of the communities (Site 4 2019 and Site 4 2021 [zone 16]). The dominance of aerobic microorganisms explains the absence of functional groups such as sulfate-reducers and methanogenic archaea, which harbor numerous hydrogenotrophs. The absence of methanogens is consistent with the non-detection of methane during gas analyses. Laboratory tests have shown no H_2 consumption in either anaerobiosis or aerobiosis. The absence of photosynthetic or hydrogenotrophic autotrophic organisms raises the question of maintenance in such ecosystems, in particular for the communities at Site 4 2021 (zone 13 and zone 15). However, some members of the Nitrososphaeria class have been shown to be thermophilic autotrophic ammonia-oxidizers (Hatzenpichler *et al.*, 2008). This capacity would explain the very strong dominance of these kinds of archaea (up to 79% of the relative abundance), since they would be key players in the microbial communities, capable of using ammonium as an electron donor, oxygen as electron acceptor, and CO_2 as a carbon source.

It remains to evaluate the internal reactions of the iron-rich minerals of different basalts in order to conclude whether enrichment of the H_2 phase at depth is likely to be possible. Based on the Mössbauer data, we were able to establish remnant H_2 generation using the calculations of Geymond *et al.* (2022). These results give an idea of the maximum H_2 potential of the rock if the corresponding minerals undergo the associated reaction. From the reactions presented in the introduction and based on the minerals present in the basalts of the Asal–Ghoubbet rift, two main groups of reactions can be isolated: pyritization reactions involving H_2S oxidation and Fe^{3+} reduction; and reactions involving H_2O reduction and Fe^{2+} oxidation.

Fe^{3+} reduction and pyritization:



Fe^{2+} oxidation:



According to Figure 15, H_2 production is low in the upper part of the wells, *i.e.*, in the basalts of the Asal Series, with only pyritization processes occurring (up to 90 mmol/kg rock). Conversely, H_2 concentrations are much higher in the Stratoid Basalts. Pyritization of magnetite (up to 486 mmol/kg rock) and oxidation of chlorite (up to 1332 mmol/kg rock) are the two processes leading to the highest H_2 production. It can be seen that olivine alteration and hematization do not offer high hydrogen generation potential in this setting, with olivine content being very low in these basalts. The presence of iron-rich chlorite at depth also offers interesting potential for the production of H_2 , if of course all of the Fe^{2+} becomes Fe^{3+} . To investigate this possibility further, we assumed the maximum point at 1332 mmol/kg of rock to be equivalent to approximately 32.04 L/kg of H_2 (at 20 °C and 1 atm). If we consider a redox cycle where iron is both reduced and oxidized under optimal conditions, where all iron reacts to form H_2 , the remnant H_2 production of these basalts from the F1 and Glc1 wells is, respectively 211.5 and 197 mmol/kg for the Asal Series basalts and 1192 and 304.2 mmol/kg for the Stratoid Series basalts.

This difference between the two series can be explained by the high Fe^{3+} content of the basalts of the Asal Series, even though the alteration index is lower. The concentrations of magnetite and hematite (maghemite and ferrihydrite, intermediate iron oxides), where Fe^{3+} is contained, are lower than Fe^{2+} -minerals in basalts; accordingly, the reduction reactions of this iron that can generate H_2 are lower than the oxidation reactions. It can be argued that the latter basaltic units were formed in a more oxidizing environment in direct contact with the

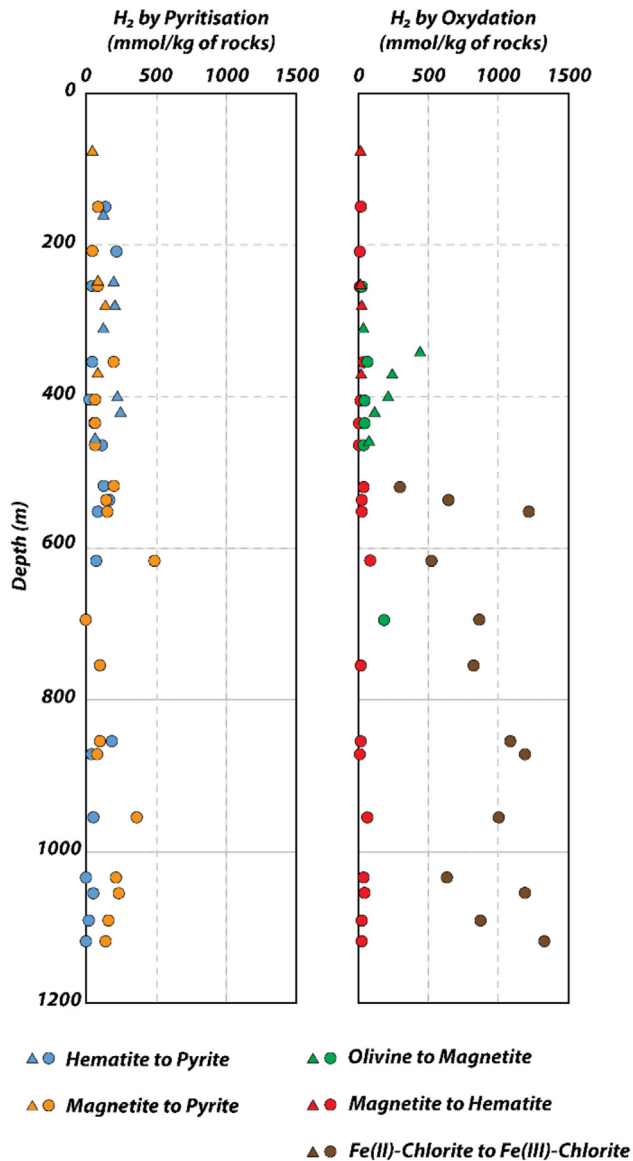


Fig. 15. Remnant potential of rocks as a function of depth according to different redox reactions and based on Mössbauer analyses. Glc1 (triangles) and F1 (dots).

atmosphere. However, in the Asal Series, the remaining Fe^{2+} is mainly concentrated in Fe-clinopyroxene, which is has much slower H_2 formation kinetics than olivine or oxides and does not easily integrate Fe^{3+} in its structure.

4.4 H₂ system

A hydrogen system, as in a petroleum system, is defined by the source rock, reservoir, a seal and the migration pathways between these elements. Here, we discuss likely candidates for each of these components.

4.4.1 Source

There is not a single source; we were able to distinguish a primary volcanic source produced by degassing of the magma chamber under the Fiale Caldera, with a summit identified at 3–5 km depth in the rift axis (Doubré *et al.*, 2007). In volcanic areas, the major gases present are H_2O , CO_2 , and S phases (Giggenbach, 1996). Thus, during degassing, H_2 is controlled by the SO_2 – H_2S equilibrium and formed mainly *via* the reaction $\text{H}_2\text{O} + \text{H}_2\text{S} = \text{SO}_2 + \text{H}_2$ (Klein *et al.*, 2020). Little H_2S has been observed at the surface in fumaroles (Pasquet *et al.*, 2021), suggesting that it has interacted with water to form H_2 and SO_2 or sulfides. Pyrite is observed in our sample 30 and in all other Asal wells (Zan *et al.*, 1990). Otherwise, because SO_2 and H_2S are extremely soluble in the aqueous phase, SO_4 may have been formed.

The two other possible sources are related to rock–fluid interactions. The remnant potential of these sources has been calculated for an ideal case where the whole iron-rich mineral undergoes a redox reaction. This provides an indication of the maximum potential remaining for H_2 generation. Fe^{3+} reduction (or pyritization), as described in the previous section, involves iron minerals such as hematite (and maghemite) and magnetite reacting with H_2S partly from degassing to form pyrite and H_2 . The presence of pyrite as revealed by XRD and Mössbauer analyses (Fig. 9) supports this hypothesis, although the small quantities measured suggest that this is not the major source of H_2 (or the source with the greatest potential). In sample 30 from well Fiale 1, Fe^{2+} -pyrite represents 17% of the iron content (Tab. 2), with a total iron concentration of 8.62 wt% in the sample, pyrites represent 1.47 wt% of the sample.

Secondly, hydrothermal reactions involving olivine, magnetite, or chlorite alteration by water reduction are associated with the oxidation of Fe^{2+} to Fe^{3+} . Although not measured (H_2 content) at depth in the rift axis wells during drilling, this source (and particularly the oxidation of Fe-chlorite in the Stratoïd Basalts deeper than 552 m) has the greatest hydrogen generation potential (with an average of 1192 mmol H_2 /kg rock in the Stratoïd Series basalts) (Fig. 15). Dehydrogenation chlorite processes occur systematically and differ based on the chlorite type, one oxidize Fe^{2+} gives one H^+ (Stuedel *et al.*, 2016). Optimum dehydrogenation for Fe^{2+} -rich chlorite, like our case, were calculated on a range between 390 °C and 410 °C (Lempart *et al.*, 2018). This zone corresponds to the geothermal propylitic zone (chlorite–epidote assemblage). Olivine does not play a major role here, in contrast to what has been observed at the Mid Atlantic Ridge or in other ophiolitic contexts (Vacquand *et al.*, 2018). In the Asal Series, according to the cuttings, olivine represents 0.1 to 0.5 wt% of the rocks and 1.6 wt% for sample 30. However, in terms of volume, it should be noted that the volume of H_2 that could be generated in this area is considerable. Based on an average value of 500 mmol H_2 /kg, *i.e.* 1 g H_2 /kg of rock (by averaging the values obtained from the reactions in Fig. 15) over a thickness of 500 m (according to the occurrence of chlorite by XRD in Figure 13, to be in the propylitic zone in well Fiale 1),. Even a “small” area, such as the Fiale Caldera

between Ghoubbet Bay and Lake Asal ($\sim 25 \text{ km}^2$), could produce up to 20 Mt of H_2 . Globally, one may then consider that the main focus of future exploration should be the detection of reservoirs and seals.

4.4.2 Reservoir

A good reservoir must have a well-connected porosity and some permeability.

As already noted, different volcanic units have been identified at depth, ranging from the Asal Series Basalts to the Stratoïd Basalts and Dahla Basalts (Varet, 1978). Although mineralogically similar, these transitional fissural basalts have a rather high primary porosity of approximately 10% (Aquater, 1989). This porosity can be explained by degassing during the emplacement of the lava flow but it does not imply that it is connected. Pasquet *et al.* (2021) also showed that there was porosity in the vicinity of the phenocrysts in the microlithic texture, through which the primary gases could flow forming these flames like hematite bodies in olivines.

Physical parameters including porosity and large scale permeability were measured during the various drilling campaigns. In the rift axis, at wells A4, A5, F1, F2, and F3, permeability was found to be rather low (Houssein and Axelsson, 2010), with values $< 1.5 \text{ mD}$ in well A5 (Elmi, 2005). Nevertheless, cold fluid circulation ($\sim 60^\circ\text{C}$) has been observed at depths between 600 and 1200 m in the Stratoïd Basalts, in the axis wells (Zan *et al.*, 1990), and has been interpreted as marine intrusion. Greater permeability has been measured at the outer margins, in wells A3 and A6 (Abdillahi, 2014): between 10 and 50 mD in well A3 (near well Glc1) at depths of 1016–1316 m which corresponds to the propylitic zone according to the XRD (Elmi, 2005; Houssein and Axelsson, 2010), and thus within the Dahla Series (D'Amore *et al.*, 1997). This permeability originated from the fractures and the interbeds between the lava flows (Zan *et al.*, 1990). Temperatures measured in these permeable zones are approximately 260°C (Zan *et al.*, 1990; Elmi, 2005). Furthermore, the extensional activity of the rift induces local high vertical permeability, as evidenced by the surface fumaroles on the major rift faults (Pasquet *et al.*, 2021).

4.4.3 Seal

The various wells studied to date, both in the rift axis and along the margins, exhibit a strong increase in temperature associated with low resistivity ($1.9 \Omega\cdot\text{m}$) at depths between 240 and 600 m (Zan *et al.*, 1990; Varet, 2014). This layer is interpreted as a relatively continuous clay-rich layer that may represent the seal of a geothermal reservoir (Varet, 2014). Figure 13 highlights the sharp increase in temperature from 30°C to 210°C over these 360 m, that means a low thermal conductivity zone. It is in agreement with the rheology since the basalts have a conductivity around $3 \text{ W}\cdot\text{m}^{-1}\text{K}^{-1}$ and the shales around $1.7 \text{ W}\cdot\text{m}^{-1}\text{K}^{-1}$. In the likely hypothesis of a thermal field mainly due to the fluid advection, cold as hot, this sharp increase suggests, as the low resistivity, a low permeability zone. This thermal field is not in steady state as confirmed by the fact that the cold zone is a consequence of the Ardoukoba event (1978–1987 period), also recent magmatic injections between 1991 and 2001, resulted in

some heating events (Varet, 2014). The XRD and bulk analysis results reported in this study indicate the presence of smectite at these depths. The LOI results confirm this smectite-rich horizon in well F1 along the rift axis, at depths between 0 and 500 m ($\text{LOI}_{\text{smectite}} < \text{LOI}_{\text{chlorite}}$ [Sun *et al.*, 2009]). In Glc1, a very altered layer dominated by hyaloclastites was observed at the top of the well with smectites below, with LOI decreasing progressively to 500 m depth (the limit of the well). With a thermal cap, a very low gradient zone is observed, at 130°C (Fig. 13). In the literature the geothermal argillic zones are characterized by a dominant smectite composition with associated minerals such as calcite, zeolites or hematite, marked by temperatures below 180°C and resistivities below $10 \Omega\cdot\text{m}$ (Henley and Ellis, 1983; Stimac *et al.*, 2008). It corresponds to the geothermal reservoir seal.

Thus, despite the notable contribution of argillization to decreasing porosity and permeability, we cannot confirm that a seal for a geothermal reservoir is also a seal for a H_2 reservoir. But if so, such a seal would be more likely present in well Glc1, along the outer margin, over 450 m deep ($\text{LOI} > 11\%$) than in well F1 and therefore in the rift axis.

Resistivity and temperature analyses have indicated a potential seal between 0 and 500 m. The main issues yet to be resolved include the definition of the minimum clay content required to form a H_2 seal and the confirmation of whether a geothermal reservoir seal can be considered equivalent to an H_2 seal. So far 3 types of hydrogen reservoir seal have been described, namely the dolerite in the Mali wells (Prinzhofer *et al.*, 2018), the clays of the Mid-Rift system in Kansas (Coveney *et al.*, 1987; Guélard *et al.*, 2017) and the salt layer in the Amadeus basin (Leila *et al.*, 2022).

4.4.4 Migration

The poorly connected porosity and low permeability of basalts makes the circulation of gases complex. Gases will typically seek preferential paths along major or minor active faults (*i.e.*, rather vertical permeability; Fig. 16) or along the strata boundaries of basalt flows (*i.e.*, horizontal permeability). The presence of vertical fast migration pathways is evidenced by the fumaroles on the surface along the faults and the absence of H_2 in the basaltic floor of the rift axis (Fig. 2) (Pasquet *et al.*, 2021).

5 Conclusions

5.1 Hydrothermal system in a young spreading center

Many authors working on MORs have highlighted the differences between the basalts and the olivine-rich upper mantle in terms of H_2 generation and have shown that hydrothermal vent fluid composition is largely controlled by oceanic lithosphere composition (see, for instance, Wetzel and Shock (2000) and references therein). Studies of the evolution of fresh basalts with depth at MORs are less numerous and the one presented here both allows a closer view of alteration over the first few million years and discusses the influence of deep fluids *versus* those arising from water/rock interactions within the final gases.

Our data proves that the gases in the Asal–Ghoubbet rift are still mainly volcanic in origin, corresponding to the degassing of the magmatic chamber (Holloway and O'Day,

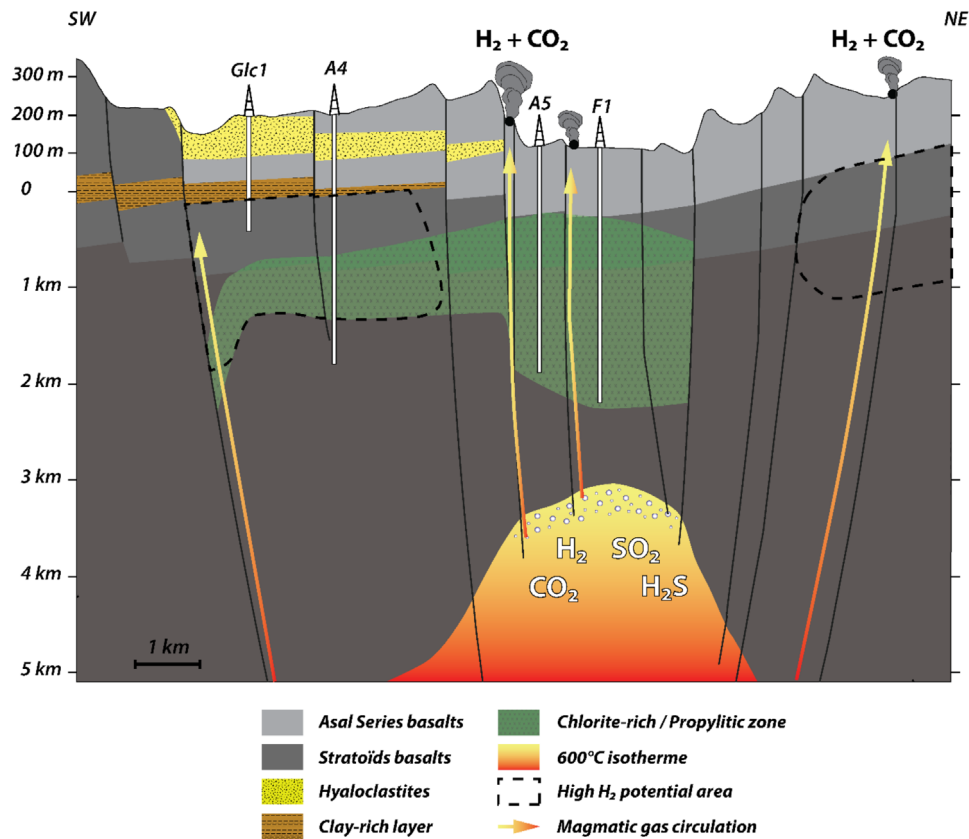


Fig. 16. Schematic diagram of the geothermal and potential H_2 zones of the Asal–Ghoubbet rift.

2000); CO_2 makes up the majority, but H_2S reduction is likely to generate some H_2 in that process. The elevated heat flows in the rift induce rapid circulation of water and steam, which enhances basalt weathering. The resulting water/rock interactions will result in water reduction, although low quantities of olivine are present in the basaltic series of the Asal Rift. However, the alteration of basalt leads to the formation of clay; the resulting Fe-rich chlorite may then be oxidized and generate additional H_2 .

The alteration profile of the basalt of the Asal–Ghoubbet Rift is consistent with typical alteration in high-temperature geothermal fields. Furthermore, the first hundred meters of rock below the surface are already altered at the rift margins, with LOI reaching 17% for basalts with ages of less than 1 Ma, and slightly weathered along the axis. This indicates that seawater was present and then removed during the accretion of the subsequent basalt flows. In this context, we have provided an overview of underwater, meteoric, and atmospheric alteration/oxidation over depths of a few kilometers. Here, the contacts between the basalt and the air and the oxygen-rich seawater have exerted a strong influence over this evolution.

5.2 Representativeness of the surface data

The data recorded from Site 4, an emitting fracture related to the major faults that border the rift to the southwest, indicate the

presence of H_2 . The concentration of H_2 here varies from 400 to 1000 ppm, although our sensor saturated at 1000 ppm; after air correction, our data indicate 0.5 to 3% H_2 . This value is not uniform; however, global variations in the value are smaller than the variations detected in soil affected by microseepage of H_2 in the continental domain (Prinzhofer *et al.*, 2019; Moretti *et al.*, 2021, 2022). This is coherent with the differences between micro- and macro-seepages observed for the natural gas, which reflect differences in the mode of transport of hydrogen through soils and fractures (Schumacher, 1996). The velocity of the fluid within fractures is greater than that in soil; faster fluid flow reduces the potential for interaction and, in our case, reduces the rate of H_2 consumption by chemical or microbiological reactions. This means that a few measurements may be sufficient to determine if a fracture emits H_2 and that long-term monitoring is not mandatory, as it is for the H_2 -emitting fairy circles in the cratons.

In this case study, microorganisms can be considered to have an indirect impact on H_2 . Indeed, it is known that NH_3 and NH_4 are present in volcanic gases and that, *via* interaction with water and/or iron, redox reactions occur and can form both N_2 and H_2 . The presence of these gases in fumaroles may explain the presence of ammonia-oxidizing archaea; further investigation could confirm the mechanisms underlying the high N_2 content of the emission zone at Site 4 (if we assume that the balance consists primarily of N_2).

5.3 H₂ potential in the Fiale area

The gas data demonstrates the presence of H₂ in the well on the margin of the rift. However, although the fumaroles at the center of the rift contain H₂, no H₂ was detected at depth in this area (*i.e.*, in the A5 and F1 wells) during drilling, because of the absence of measurements. At the opposite, on the margin near Glc1, H₂ concentrations were very low at the surface. The other difference between the central axis and the margins relates to the presence of a geothermal gradient inversion due to the flow of seawater from Ghoubbet Bay to Lake Asal. In addition, alteration of the basalts along the rift margins led to the formation of hyaloclastites and smectites, which may constitute a potential seal for both geothermal reservoirs and H₂. Although diffuse, the H₂ potential (in terms of theoretical volume) is large: more than 500 mmol H₂/kg rock. The majority of this H₂ may have been lost by continuous leakage to the surface. However, accumulations (even temporary ones) may still occur in cases where a reservoir and seal are present. Such a reservoir would be preferentially located at depths of 1000–1300 m on the southwestern rift margin, in the Dahla Basalts, zone with the best permeability (10–50 mD). This zone is located in the propylitic geothermal zone (chlorite–epidote assemblage) and it's also a potential source of H₂ through Fe²⁺ oxidation and chlorite dehydrogenation (Fig. 16). The outer margins of North Ghoubbet can also be considered prospective in this context but data are still scarce in this area without well.

Thermodynamic calculations must now be carried out to better constrain the reaction kinetics in these ferrous chlorites. Furthermore, despite the surface and well data on H₂ in the margins, can this poorly connected porosity make these basalts a good reservoir. Further experimental studies are also needed to improve the documentation of H₂ seals.

Acknowledgements. We thank Isotope Editing for editing a draft of this manuscript. We thank ODDEG for sharing with us their knowledge of Djibouti geology and for allowing us access to the cuttings from the two studied wells. This collaboration, ODDEG-UPPA, was initiated by K Moussad, J Varet, and I Moretti.

I would like to thank Alain Prinzhofer, Yves Geraud and an anonymous reviewer for their constructive comments which helped to clarify this article.

Funding

G.P.'s PhD was funded by the Isite E2S; the fieldwork was funded by the Carnot ISIFOR. Amin Mohamed Idriss is now studying in UPPA thanks to Campus France.

Supplementary material

Table of raw gas measurements done at the Asal-Ghoubbet drift site 4 on 21/11/19, 12/08/19 and 13/08/19.

The Supplementary material is available at <https://www.bsgf.fr/10.1051/bsgf/2023004/olm>.

References

- Abdillahi MM. 2014. Predicting output curves for deep wells in Asal Rift, Djibouti. UNU-GTP 22.
- Abrajano TA, Sturchio NC, Bohlke JK, Lyon GL, Poreda RJ, Stevens CM. 1988. Methane-hydrogen gas seeps, Zambales Ophiolite, Philippines: deep or shallow origin? *Chemical Geology* 71: 211–222. [https://doi.org/10.1016/0009-2541\(88\)90116-7](https://doi.org/10.1016/0009-2541(88)90116-7).
- Ahmed MM. 2018. Well design for the Asal geothermal field: a case study for well Glc-2. UNU-GTP 20.
- Allard P, Tazieff H, Dajlevic D, 1979. Observations of seafloor spreading in Afar during the November 1978 fissure eruption. *Nature* 279: 30–33. <https://doi.org/10.1038/279030a0>.
- Al Saade K, Ashy R, Al-Fassi F, Al Judaibi A. 2022. Microbial diversity and abundance in the hot springs on the west coast of Saudi Arabia as a potential source of novel industrial products. *MBJ* 7: 8–17. <https://doi.org/10.21608/mb.2022.134787.1055>.
- Ansary MMS, Ahmadimoghadam A, Mirtadzadini SM. 2017. Distribution of cyanobacteria in two sirch hot springs with regards to the physicochemical traits of water. *Banat's Journal of Biotechnology* 8: 83–89. [https://doi.org/10.7904/2068-4738-VIII\(15\)-83](https://doi.org/10.7904/2068-4738-VIII(15)-83).
- Aquater. 1989. Djibouti geothermal exploration project, Republic of Djibouti: final report. Government of Djibouti, ISERST 159.
- Arif S, Willenberg C, Dreyer A, Nacke H, Hoppert M. 2021. Sasso Pisano geothermal field environment harbours diverse Ktedonobacteria representatives and illustrates habitat-specific adaptations. *Microorganisms* 9: 1402. <https://doi.org/10.3390/microorganisms9071402>.
- Ármannsson H, Benjamínsson J, Jeffrey AWA. 1989. Gas changes in the Krafla geothermal system, Iceland. *Chemical Geology* 76: 175–196. [https://doi.org/10.1016/0009-2541\(89\)90089-2](https://doi.org/10.1016/0009-2541(89)90089-2).
- Arrouvel C, Prinzhofer A. 2021. Genesis of natural hydrogen: new insights from thermodynamic simulations. *International Journal of Hydrogen Energy* 46: 18780–18794. <https://doi.org/10.1016/j.ijhydene.2021.03.057>.
- Barberi F, Ferrara G, Santacroce R, Treuil M, Varet J. 1975a. A transitional basalt-pantellerite sequence of fractional crystallization, the Boina Centre (Afar Rift, Ethiopia). *Journal of Petrology* 16: 22–56. <https://doi.org/10.1093/petrology/16.1.22>.
- Barberi F, Ferrara G, Santacroce R, Varet J. 1975b. Structural evolution of the Afar triple junction. 1: 38–54. <https://doi.org/10.1086/627797>.
- Barberi F, Tazieff H, Varet J. 1972. Volcanism in the Afar depression—its tectonic and magmatic significance. *Tectonophysics* 15: 19–29. [https://doi.org/10.1016/0040-1951\(72\)90046-7](https://doi.org/10.1016/0040-1951(72)90046-7).
- Barberi F, Varet J. 1977. Volcanism of Afar: small-scale plate tectonics implications. *GSA Bulletin* 88: 1251–1266. [https://doi.org/10.1130/0016-7606\(1977\)88<1251:VOASPT>2.0.CO;2](https://doi.org/10.1130/0016-7606(1977)88<1251:VOASPT>2.0.CO;2).
- Barberi F, Varet J. 1970. The Erta Ale volcanic range (Danakil depression, northern Afar, Ethiopia). *Bull Volcanol* 34: 848–917. <https://doi.org/10.1007/BF02596805>.
- Boreham CJ, Sohn JH, Cox N, Williams J, Hong Z, Kendrick MA. 2021. Hydrogen and hydrocarbons associated with the Neorachean Frog's Leg Gold Camp, Yilgarn Craton, Western Australia. *Chemical Geology* 575: 120098. <https://doi.org/10.1016/j.chemgeo.2021.120098>.
- Brindley GW, Youell RF. 1953. Ferrous chamosite and ferric chamosite. *Mineral Mag J Mineral Soc* 30: 57–70. <https://doi.org/10.1180/minmag.1953.030.220.07>.
- Charlou JL, Donval JP, Fouquet Y, Jean-Baptiste P, Holm N. 2002. Geochemistry of high H₂ and CH₄ vent fluids issuing from ultramafic rocks at the Rainbow hydrothermal field (36°14'N, MAR). *Chemical Geology* 191: 345–359. [https://doi.org/10.1016/S0009-2541\(02\)00134-1](https://doi.org/10.1016/S0009-2541(02)00134-1).

- Charlou JL, Fouquet Y, Bougault H, Donval JP, Etoubleau J, Jean-Baptiste P, *et al.* 1998. Intense CH₄ plumes generated by serpentinization of ultramafic rocks at the intersection of the 15°20'N fracture zone and the Mid-Atlantic Ridge. *Geochimica et Cosmochimica Acta* 62: 2323–2333. [https://doi.org/10.1016/S0016-7037\(98\)00138-0](https://doi.org/10.1016/S0016-7037(98)00138-0).
- Combaudon V, Moretti I, Kleine BI, Stefánsson A. 2022. Hydrogen emissions from hydrothermal fields in Iceland and comparison with the Mid-Atlantic Ridge. *International Journal of Hydrogen Energy* 47: 10217–10227. <https://doi.org/10.1016/j.ijhydene.2022.01.101>.
- Coveney J, Raymond, Goebel ED, Zeller EJ, Dreschhoff GAM, Angino EE. 1987. Serpentinization and the origin of hydrogen gas in Kansas. *The American Association of Petroleum Geologists Bulletin* 71: 39–48. <https://doi.org/10.1306/94886D3F-1704-11D7-8645000102C1865D>.
- D'Amore F, Giusti D, Abdallah A. 1997. Geochemistry of the high-salinity geothermal field of Asal, Republic of Djibouti, Africa. *Geothermics* 27: 197–210. [https://doi.org/10.1016/S0375-6505\(97\)10009-8](https://doi.org/10.1016/S0375-6505(97)10009-8).
- Delibrias G, Marinelli G, Stieltjes L. 1975. Spreading rate of the Asal Rift: a geological approach, Afar Depression of Ethiopia.
- Demange J, Stieltjes L, Varet J. 1980. L'éruption d'Asal de novembre 1978. *Bulletin de la Société géologique de France S7-XXII*: 837–843. <https://doi.org/10.2113/gssgfbull.S7-XXII.6.837>.
- Deville E, Prinzhofer A. 2016. The origin of N₂-H₂-CH₄-rich natural gas seepages in ophiolitic context: a major and noble gases study of fluid seepages in New Caledonia. *Chemical Geology* 440: 139–147
- Dodsworth JA, Gevorkian J, Despujos F, Cole JK, Murugapiran SK, Ming H, *et al.* 2014. *Thermoflexus hugenholtzii* gen. nov., sp. nov., a thermophilic, microaerophilic, filamentous bacterium representing a novel class in the *Chloroflexi*, *Thermoflexia classis* nov., and description of *Thermoflexaceae* fam. nov. and *Thermoflexales* ord. nov. *International Journal of Systematic and Evolutionary Microbiology* 64: 2119–2127. <https://doi.org/10.1099/ijs.0.055855-0>.
- Dobre C, Manighetti I, Dorbath C, Dorbath L, Jacques E, Delmond JC. 2007. Crustal structure and magmato-tectonic processes in an active rift (Asal-Ghoubbet, Afar, East Africa): 1. Insights from a 5-month seismological experiment. *J Geophys Res* 112: B05405. <https://doi.org/10.1029/2005JB003940>.
- Dobre C, Peltzer G. 2007. Fluid-controlled faulting process in the Asal Rift, Djibouti, from 8 yr of radar interferometry observations. *Geol* 35: 69. <https://doi.org/10.1130/G23022A.1>.
- Elmi D. 2005. Analysis of geothermal well test data from the Asal rift area, Republic of Djibouti. UNU-GTP Reports 2005, 21.
- Fournier M, Gasse F, Lépine J-C. 1984. Carte géologique de la République de Djibouti à 1:100 000.
- Franzson H, Zierenberg R, Schiffman P. 2008. Chemical transport in geothermal systems in Iceland. *Journal of Volcanology and Geothermal Research* 173: 217–229. <https://doi.org/10.1016/j.jvolgeores.2008.01.027>.
- Gaucher EC. 2020. New perspectives in the industrial exploration for native hydrogen. *Elements* 16: 8–9. <https://doi.org/10.2138/gselements.16.1.8>.
- Geymond U, Ramanaidou E, Lévy D, Ouaya A, Moretti I. 2022. Can weathering of banded iron formations generate natural hydrogen? Evidence from Australia, Brazil and South Africa. *Minerals* 12: 163. <https://doi.org/10.3390/min12020163>.
- Giggenbach WF. 1996. Chemical composition of volcanic gases. In: *Monitoring and mitigation of volcano hazards*. Berlin, Heidelberg: Springer Berlin Heidelberg, pp. 221–256. https://doi.org/10.1007/978-3-642-80087-0_7.
- Guajardo-Leiva S, Santos F, Salgado O, Regeard C, Quillet L, Díez B. 2021. Unveiling ecological and genetic novelty within lytic and lysogenic viral communities of hot spring phototrophic microbial mats. *Microbiol Spectr* 9: e00694-21. <https://doi.org/10.1128/Spectrum.00694-21>.
- Guélard J, Beaumont V, Rouchon V, Guyot F, Pillot D, Jézéquel D, *et al.* 2017. Natural H₂ in Kansas: deep or shallow origin? *Geochemistry, Geophysics, Geosystems* 18: 1841–1865. <https://doi.org/10.1002/2016GC006544>.
- Haddad PG, Ranchou-Peyruse M, Guignard M, Mura J, Casteran F, Ronjon-Magand L, *et al.* 2022. Geological storage of hydrogen in deep aquifers—an experimental multidisciplinary study. *Energy Environ Sci* 15: 3400–3415. <https://doi.org/10.1039/D2EE00765G>.
- Hatzenpichler R, Lebedeva EV, Spieck E, Stoecker K, Richter A, Daims H, *et al.* 2008. A moderately thermophilic ammonia-oxidizing crenarchaeote from a hot spring. *Proc Natl Acad Sci U S A* 105: 2134–2139. <https://doi.org/10.1073/pnas.0708857105>.
- Havig JR, Hamilton TL. 2019. Productivity and community composition of low biomass/high silica precipitation hot springs: a possible window to earth's early biosphere? *Life* 9: 64. <https://doi.org/10.3390/life9030064>.
- Henley RW, Ellis AJ. 1983. Geothermal systems ancient and modern: a geochemical review. *Earth-Science Reviews* 19: 1–50. [https://doi.org/10.1016/0012-8252\(83\)90075-2](https://doi.org/10.1016/0012-8252(83)90075-2).
- Holloway JR, O'Day PA. 2000. Production of CO₂ and H₂ by dike-eruptive events at Mid-Ocean Ridges: implications for abiotic organic synthesis and global geochemical cycling. *International Geology Review* 42: 673–683. <https://doi.org/10.1080/00206810009465105>.
- Houssein DE, Axelsson G. 2010. Geothermal resources in the Asal Region, Republic of Djibouti: an update with emphasis on reservoir engineering studies. *Geothermics* 39: 220–227. <https://doi.org/10.1016/j.geothermics.2010.06.006>.
- Inan K, Ozer A, Ibrahim Guler H, Osman Belduz A, Canakci S. 2016. *Brevibacillus gelatini* sp. nov., isolated from a hot spring. *International Journal of Systematic and Evolutionary Microbiology* 66: 712–718. <https://doi.org/10.1099/ijsem.0.000780>.
- Kelley DS. 2005. A serpentinite-hosted ecosystem: the lost city hydrothermal field. *Science* 307: 1428–1434. <https://doi.org/10.1126/science.1102556>.
- Kelley DS, Karson JA, Blackman DK, Früh-Green GL, Butterfield DA, Lilley MD, *et al.* 2001. An off-axis hydrothermal vent field near the Mid-Atlantic Ridge at 30°N. *Nature* 412: 145–149. <https://doi.org/10.1038/35084000>.
- Klein F, Tarnas JD, Bach W. 2020. Abiotic sources of molecular hydrogen on earth. *Elements* 16: 19–24. <https://doi.org/10.2138/gselements.16.1.19>.
- Kularatne K, Sissmann O, Kohler E, Chardin M, Noirez S, Martinez I. 2018. Simultaneous ex-situ CO₂ mineral sequestration and hydrogen production from olivine-bearing mine tailings. *Applied Geochemistry* 95: 195–205. <https://doi.org/10.1016/j.apgeochem.2018.05.020>.
- Lapi T, Chatzimpiros P, Raineau L, Prinzhofer A. 2022. System approach to natural versus manufactured hydrogen: an interdisciplinary perspective on a new primary energy source. *International Journal of Hydrogen Energy* 47: 21701–21712. <https://doi.org/10.1016/j.ijhydene.2022.05.039>.
- Larin N, Zgonnik V, Rodina S, Deville E, Prinzhofer A, Larin VN. 2015. Natural molecular hydrogen seepage associated with surficial, rounded depressions on the European Craton in Russia. *Nat Resour Res* 24: 369–383. <https://doi.org/10.1007/s11053-014-9257-5>.

- Leila M, Lévy D, Battani A, Piccardi L, Šegvić B, Badurina L, *et al.* 2021. Origin of continuous hydrogen flux in gas manifestations at the Larderello geothermal field, Central Italy. *Chemical Geology* 585: 120564. <https://doi.org/10.1016/j.chemgeo.2021.120564>
- Leila M, Loiseau K, Moretti I. 2022. Controls on generation and accumulation of blended gases (CH₄/H₂/He) in the Neoproterozoic Amadeus Basin, Australia. *Marine and Petroleum Geology* 140: 105643. <https://doi.org/10.1016/j.marpetgeo.2022.105643>.
- Lempart M, Derkowski A, Luberd-Durnas K, Skiba M, Błachowski A. 2018. Dehydrogenation and dehydroxylation as drivers of the thermal decomposition of Fe-chlorites. *American Mineralogist* 103: 1837–1850. <https://doi.org/10.2138/am-2018-6541>.
- López-López O, Cerdán M, González-Siso M. 2013. Hot spring metagenomics. *Life* 3: 308–320. <https://doi.org/10.3390/life3020308>.
- Malvoisin B, Brunet F. 2023. Barren ground depressions, natural H₂ and orogenic gold deposits: spatial link and geochemical model. *Science of the Total Environment* 856: 158969. <https://doi.org/10.1016/j.scitotenv.2022.158969>.
- Marín-Paredes R, Tapia-Torres Y, Martínez-Romero E, Quesada M, Servín-Garcidueñas LE. 2021. Metagenome assembly and metagenome-assembled genome of “*Candidatus Aramenus sulfurataquae*” from thermal sediments from the Los Azufres volcanic complex. *Microbiol Resour Announc* 10: e00379–21. <https://doi.org/10.1128/MRA00379-21>.
- Mlynarski M, Zlotnicki J. 2001. Fluid circulation in the active emerged Asal rift (east Africa, Djibouti) inferred from self-potential and Telluric-Telluric prospecting. *Tectonophysics* 339: 455–472. [https://doi.org/10.1016/S0040-1951\(01\)00127-5](https://doi.org/10.1016/S0040-1951(01)00127-5).
- Moretti I. 2019. H₂: energy vector or source? *Actualite Chimique* 442: 15–16.
- Moretti I, Geymond U, Pasquet G, Aimar L, Rabaute A. 2022. Natural hydrogen emanations in Namibia: field acquisition and vegetation indexes from multispectral satellite image analysis. *International Journal of Hydrogen Energy* 47: 35588–35607. <https://doi.org/10.1016/j.ijhydene.2022.08.135>.
- Moretti I, Prinzhofer A, Françaolin J, Pacheco C, Rosanne M, Rupin F, *et al.* 2021. Long-term monitoring of natural hydrogen superficial emissions in a Brazilian cratonic environment. Sporadic large pulses versus daily periodic emissions. *International Journal of Hydrogen Energy* 46: 3615–3628. <https://doi.org/10.1016/j.ijhydene.2020.11.026>.
- Moretti I, Webber ME. 2021. Natural hydrogen: a geological curiosity or the primary energy source for a low-carbon future. *Renewable Matter* 34: 6.
- Neal C, Stanger G. 1983. Hydrogen generation from mantle source rocks in Oman. *Earth and Planetary Science Letters* 66: 315–320. [https://doi.org/10.1016/0012-821X\(83\)90144-9](https://doi.org/10.1016/0012-821X(83)90144-9).
- Ningsih F, Yokota A, Sakai Y, Nanatani K, Yabe S, Oetari A, *et al.* 2019. *Gandjariella thermophila* gen. nov., sp. nov., a new member of the family Pseudonocardiaceae, isolated from forest soil in a geothermal area. *International Journal of Systematic and Evolutionary Microbiology* 69: 3080–3086. <https://doi.org/10.1099/ijsem.0.003594>.
- Nonn C, Leroy S, Khanbari K, Ahmed A. 2017. Tectono-sedimentary evolution of the eastern Gulf of Aden conjugate passive margins: narrowness and asymmetry in oblique rifting context. *Tectonophysics* 721: 322–348. <https://doi.org/10.1016/j.tecto.2017.09.024>.
- Nonn C, Leroy S, Lescanne M, Castilla R. 2019. Central Gulf of Aden conjugate margins (Yemen-Somalia): Tectono-sedimentary and magmatism evolution in hybrid-type margins. *Marine and Petroleum Geology* 105: 100–123. <https://doi.org/10.1016/j.marpetgeo.2018.11.053>.
- Oskarsson N. 1984. Monitoring of fumarole discharge during the 1975–1982 rifting in Krafla volcanic center, north Iceland. *Journal of Volcanology and Geothermal Research* 22: 97–121. [https://doi.org/10.1016/0377-0273\(84\)90036-2](https://doi.org/10.1016/0377-0273(84)90036-2).
- Panosyan H, Margaryan A, Birkeland N-K. 2020. Geothermal springs in Armenia and Nagorno-Karabakh: potential sources of hydrolase-producing thermophilic bacilli. *Extremophiles* 24: 519–536. <https://doi.org/10.1007/s00792-020-01173-1>.
- Pasquet G. 2023. Évolution des gaz associés à l’ouverture des rifts, hydrogène naturel et autres. Cas du rift est-africain (PhD thesis). Université de Pau et des Pays de l’Adour.
- Pasquet G, Combaudon V, Moretti I. 2022. Génération d’hydrogène par les jeunes croûtes océaniques : les cas de l’Islande et de la zone de l’Afar. *Hydrogène et gaz rares Géologues*: 74–78.
- Pasquet G, Houssein Hassan R, Sissmann O, Varet J, Moretti I. 2021. An attempt to study natural H₂ resources across an Oceanic Ridge penetrating a continent: the Asal-Ghoubbet Rift (Republic of Djibouti). *Geosciences* 12: 16. <https://doi.org/10.3390/geosciences12010016>.
- Prinzhofer A, Moretti I, Françaolin J, Pacheco C, D’Agostino A, Werly J, *et al.* 2019. Natural hydrogen continuous emission from sedimentary basins: the example of a Brazilian H₂-emitting structure. *International Journal of Hydrogen Energy* 44: 5676–5685. <https://doi.org/10.1016/j.ijhydene.2019.01.119>.
- Prinzhofer A, Tahara Cissé CS, Diallo AB. 2018. Discovery of a large accumulation of natural hydrogen in Bourakebougou (Mali). *International Journal of Hydrogen Energy* 43: 19315–19326. <https://doi.org/10.1016/j.ijhydene.2018.08.193>.
- Reed MH, Palandri J. 2008. Hydrogen Produced by reduction of H₂O in rock reaction: peridotite vs basalt. In: AIP Conference Proceedings. Presented at the 2007, AIP, Sendai (Japan), pp. 100–104. <https://doi.org/10.1063/1.2896951>.
- Rigollet C, Prinzhofer A. 2022. Natural hydrogen: a new source of carbon-free and renewable energy that can compete with hydrocarbons. *First Break* 40: 78–84. <https://doi.org/10.3997/1365-2397.fb2022087>.
- Sano Y, Urabe A, Wakita H, Wushiki H. 1993. Origin of hydrogen-nitrogen gas seeps, Oman. *Applied Geochemistry* 8: 1–8. [https://doi.org/10.1016/0883-2927\(93\)90053-J](https://doi.org/10.1016/0883-2927(93)90053-J).
- Schumacher D. 1996. Hydrocarbon-induced alteration of soils and sediments. In: Schumacher D, Abrams MA, eds. Hydrocarbon migration and its near-surface expression. American Association of Petroleum Geologists, pp. 0. <https://doi.org/10.1306/M66606C6>.
- Sissmann O, Brunet F, Martínez I, Guyot F, Verlaquet A, Pinquier Y, *et al.* 2014. Enhanced olivine carbonation within a basalt as compared to single-phase experiments: reevaluating the potential of CO₂ mineral sequestration. *Environ Sci Technol* 48: 5512–5519. <https://doi.org/10.1021/es405508a>.
- Smith NJP, Shepherd TJ, Styles MT, Williams GM. 2005. Hydrogen exploration: a review of global hydrogen accumulations and implications for prospective areas in NW Europe. *Petroleum Geology Conference Series* 6: 349–358. <https://doi.org/10.1144/0060349>.
- Smrhova T, Jani K, Pajer P, Kapinusova G, Vylita T, Suman J, *et al.* 2022. Prokaryotes of renowned Karlovy Vary (Carlsbad) thermal springs: phylogenetic and cultivation analysis. *Environmental Microbiome* 17: 48. <https://doi.org/10.1186/s40793-022-00440-2>.
- Studel A, Kleeberg R, Koch CB, Friedrich F, Emmerich K. 2016. Thermal behavior of chlorites of the clinocllore-chamosite solid solution series: oxidation of structural iron, hydrogen release and dehydroxylation. *Applied Clay Science* 132–133: 626–634. <https://doi.org/10.1016/j.clay.2016.08.013>.
- Stevens TO, McKinley JP. 2000. Abiotic controls on H₂ production from basalt-water reactions and implications for aquifer biogeochemistry. *Environ Sci Technol* 34: 826–831. <https://doi.org/10.1021/es990583g>.

- Stevens TO, McKinley JP. 1995. Lithoautotrophic microbial ecosystems in deep basalt aquifers. *Science* 270: 450–454. <https://doi.org/10.1126/science.270.5235.450>.
- Stieltjes L, Joron JL, Treuil M, Varet J. 1976. Le rift d'Asal, segment de dorsale émerge; discussion pétrologique et géochimique. *Bulletin de la Société géologique de France* S7-XVIII: 851–862. <https://doi.org/10.2113/gssgfbull.S7-XVIII.4.851>.
- Stimac J, Nordquist G, Suminar A, Sirad-Azwar L. 2008. An overview of the Awibengkok geothermal system, Indonesia. *Geothermics* 37: 300–331. <https://doi.org/10.1016/j.geothermics.2008.04.004>.
- Sun H, Nelson M, Chen F, Husch J. 2009. Soil mineral structural water loss during loss on ignition analyses. *Can J Soil Sci* 89: 603–610. <https://doi.org/10.4141/CJSS09007>.
- Truche L, McCollom TM, Martinez I. 2020. Hydrogen and abiotic hydrocarbons: molecules that change the world. *Elements* 16: 13–18. <https://doi.org/10.2138/gselements.16.1.13>.
- Turk J, Haizlip J, Mohamed J, Mann M, Letvin A, Moussa N. 2019. A comparison of alteration mineralogy and measured temperatures from three exploration wells in the Fiale Caldera, Djibouti. *GRC Transactions* 43: 11.
- Vacquand C, Deville E, Beaumont V, Guyot F, Sissmann O, Pillot D, *et al.* 2018. Reduced gas seepages in ophiolitic complexes: evidences for multiple origins of the H₂-CH₄-N₂ gas mixtures. *Geochimica et Cosmochimica Acta* 223: 437–461. <https://doi.org/10.1016/j.gca.2017.12.018>.
- Varet J. 2014. Asal-Fialé geothermal field (Djibouti republic): a new interpretation for a geothermal reservoir in an actively spreading rift segment. In: Proceedings 5th African Rift geothermal Conference 9.
- Varet J. 1978. Carte géologique de l'Afar central et méridional (Éthiopie et T.F.A.I.).
- Wang Jiajun, Wang Jianan, Feng L, Lin T. 2015. Fluid mixing in droplet-based microfluidics with a serpentine microchannel. *RSC Adv* 5: 104138–104144. <https://doi.org/10.1039/C5RA21181F>.
- Wetzel LR, Shock EL. 2000. Distinguishing ultramafic-from basalt-hosted submarine hydrothermal systems by comparing calculated vent fluid compositions. *J Geophys Res* 105: 8319–8340. <https://doi.org/10.1029/1999JB900382>.
- Worman SL, Pratson LF, Karson JA, Schlesinger WH. 2020. Abiotic hydrogen (H₂) sources and sinks near the Mid-Ocean Ridge (MOR) with implications for the seafloor biosphere. *Proc Natl Acad Sci U S A* 117: 13283–13293. <https://doi.org/10.1073/pnas.2002619117>.
- Zan L, Gianelli G, Troisi C, Haga AO. 1990. Geothermal exploration in the Republic of Djibouti: thermal and geological data of the Hanle and Asal areas. *Geothermics* 19: 561–582. [https://doi.org/10.1016/0375-6505\(90\)90005-V](https://doi.org/10.1016/0375-6505(90)90005-V).
- Zgonnik V. 2020. The occurrence and geoscience of natural hydrogen: a comprehensive review. *Earth-Science Reviews* 203: 103140. <https://doi.org/10.1016/j.earscirev.2020.103140>.

Cite this article as: Pasquet G, Idriss AM, Ronjon-Magand L, Ranchou-Peyruse M, Guignard M, Duttine M, Ranchou-Peyruse A, Moretti I. 2023. Natural hydrogen potential and basaltic alteration in the Asal–Ghoubbet rift, Republic of Djibouti. *BSGF - Earth Sciences Bulletin* 194: 9.